Cell Genomics

Article

NRDE2 deficiency impairs homologous recombination repair and sensitizes hepatocellular carcinoma to PARP inhibitors

Graphical abstract

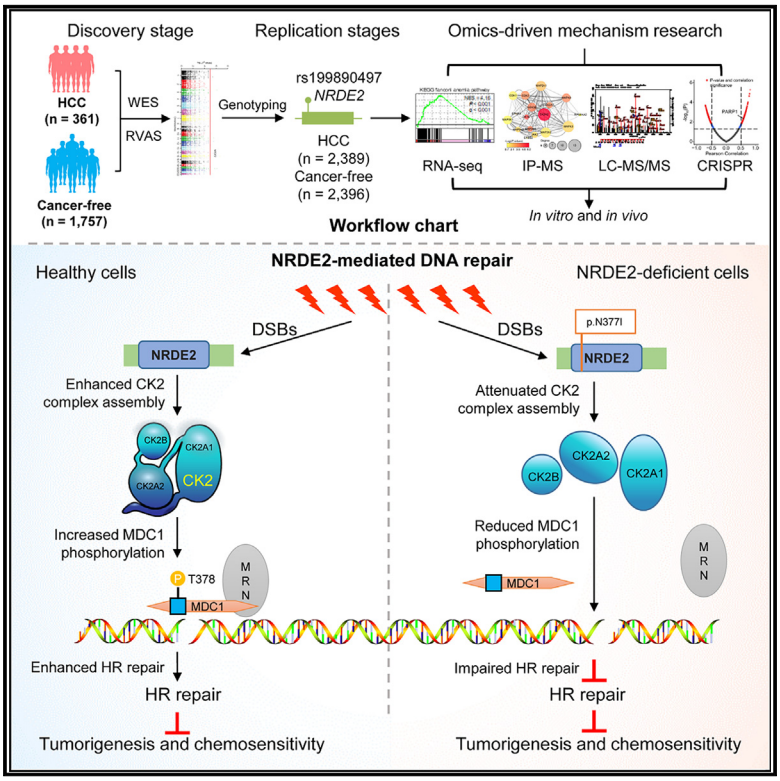

Highlights

- Rare-variant association study identifies novel HCC-associated genes, including *NRDE2*
- NRDE2 promotes HR-mediated DNA repair and plays a suppressive role in HCC
- NRDE2 facilitates CK2 holoenzyme assembly and induces the phosphorylation on MDC1
- The NRDE2 p.N377I confers a loss-of-function effect and sensitizes HCC cells to PARPi

Authors

Yahui Wang, Xinyi Liu, Xianbo Zuo, ..., Xuejun Zhang, Yuanfeng Li, Gangqiao Zhou

Correspondence

hefc@nic.bmi.ac.cn (F.H.), ayzxj@vip.sina.com (X.Z.), liyf_snp@163.com (Y.L.), zhougq114@126.com (G.Z.)

In brief

Wang et al. performed a rare-variant-based association study and identified novel genes associated with hepatocellular carcinoma risk. The authors further revealed that NRDE2 promotes homologous recombination-mediated repair and plays a tumor-suppressive role. These findings may open new avenues for treatment of hepatocellular carcinoma based on synthetic lethal effects.

Wang et al., 2024, Cell Genomics *4*, 100550
May 8, 2024
https://doi.org/10.1016/j.xgen.2024.100550

CellPress

Cell Genomics

CellPress
OPEN ACCESS

Article

NRDE2 deficiency impairs homologous recombination repair and sensitizes hepatocellular carcinoma to PARP inhibitors

Yahui Wang,[1,2,18] Xinyi Liu,[1,18] Xianbo Zuo,[3,18] Cuiling Wang,[1,18] Zheng Zhang,[1] Haitao Zhang,[1] Tao Zeng,[4] Shunqi Chen,[1] Mengyu Liu,[1] Hongxia Chen,[1] Qingfeng Song,[5] Qi Li,[1,6] Chenning Yang,[1] Yi Le,[7] Jinliang Xing,[8] Hongxin Zhang,[9] Jiaze An,[10] Weihua Jia,[11,12] Longli Kang,[13] Hongxing Zhang,[2] Hui Xie,[14] Jiazhou Ye,[15] Tianzhun Wu,[15] Fuchu He,[2,*] Xuejun Zhang,[16,*] Yuanfeng Li,[1,*] and Gangqiao Zhou[1,17,19,*]

[1]State Key Laboratory of Medical Proteomics, National Center for Protein Sciences at Beijing, Beijing Proteome Research Center, Beijing Institute of Radiation Medicine, Beijing, P.R. China

[2]State Key Laboratory of Medical Proteomics, National Center for Protein Sciences at Beijing, Beijing Proteome Research Center, Beijing Institute of Lifeomics, Beijing, P.R. China

[3]Department of Dermatology, Department of Pharmacy, China-Japan Friendship Hospital, Beijing, P.R. China

[4]Faculty of Hepato-Biliary-Pancreatic Surgery, the First Medical Center of Chinese PLA General of Hospital, Beijing, P.R. China

[5]Affiliated Cancer Hospital of Guangxi Medical University, Nanning City, Guangxi Province, P.R. China

[6]Department of Neurosciences, School of Medicine, University of South China, Hengyang City, Hunan Province, P.R. China

[7]Department of Hepatobiliary Surgery, the 5th Medical Center of Chinese PLA General of Hospital, Beijing, P.R. China

[8]State Key Laboratory of Cancer Biology, Experimental Teaching Center of Basic Medicine, Air Force Medical University, Xi'an City, Shaanxi Province, P.R. China

[9]Department of Pain Treatment, Tangdu Hospital, Air Force Medical University, Xi'an City, Shaanxi Province, P.R. China

[10]Department of Hepatobiliary Surgery, Xijing Hospital, Air Force Medical University, Xi'an City, Shaanxi Province, P.R. China

[11]State Key Laboratory of Oncology in Southern China, Guangzhou City, Guangdong Province, P.R. China

[12]Department of Experimental Research, Sun Yat-Sen University Cancer Center, Guangzhou City, Guangdong Province, P.R. China

[13]Key Laboratory for Molecular Genetic Mechanisms and Intervention Research on High Altitude Disease of Tibet Autonomous Region, Key Laboratory of High Altitude Environment and Genes Related to Diseases of Tibet Autonomous Region, School of Medicine, Xizang Minzu University, Xianyang City, Shaanxi Province, P.R. China

[14]Department of Interventional Oncology, the Fifth Medical Center of Chinese PLA General of Hospital, Beijing, P.R. China

[15]Department of Hepatobiliary & Pancreatic Surgery, Guangxi Medical University Cancer Hospital, Guangxi Liver Cancer Diagnosis and Treatment Engineering and Technology Research Center, Nanning City, Guangxi Province, P.R. China

[16]Department of Dermatology and Institute of Dermatology, First Affiliated Hospital, Anhui Medical University, Hefei City, Anhui Province, P.R. China

[17]Collaborative Innovation Center for Personalized Cancer Medicine, Center for Global Health, School of Public Health, Nanjing Medical University, Nanjing City, Jiangsu Province, P.R. China

[18]These authors contributed equally

[19]Lead contact

*Correspondence: hefc@nic.bmi.ac.cn (F.H.), ayzxj@vip.sina.com (X.Z.), liyf_snp@163.com (Y.L.), zhougq114@126.com (G.Z.)

https://doi.org/10.1016/j.xgen.2024.100550

SUMMARY

To identify novel susceptibility genes for hepatocellular carcinoma (HCC), we performed a rare-variant association study in Chinese populations consisting of 2,750 cases and 4,153 controls. We identified four HCC-associated genes, including *NRDE2*, *RANBP17*, *RTEL1*, and *STEAP3*. Using *NRDE2* (index rs199890497 [p.N377I], $p = 1.19 \times 10^{-9}$) as an exemplary candidate, we demonstrated that it promotes homologous recombination (HR) repair and suppresses HCC. Mechanistically, NRDE2 binds to the subunits of casein kinase 2 (CK2) and facilitates the assembly and activity of the CK2 holoenzyme. This NRDE2-mediated enhancement of CK2 activity increases the phosphorylation of MDC1 and then facilitates the HR repair. These functions are eliminated almost completely by the NRDE2-p.N377I variant, which sensitizes the HCC cells to poly(ADP-ribose) polymerase (PARP) inhibitors, especially when combined with chemotherapy. Collectively, our findings highlight the relevance of the rare variants to genetic susceptibility to HCC, which would be helpful for the precise treatment of this malignancy.

INTRODUCTION

Hepatocellular carcinoma (HCC) accounts for more than 75% of the total cases of primary liver cancer, which ranks the fourth leading cause of cancer-related death worldwide.[1] Understanding the molecular etiology of HCC will be substantially helpful in developing treatment strategies for this malignancy. Genetic susceptibility is considered to play critical roles in determining the risk of HCC. Recently, several candidate gene-based association studies and genome-wide association studies (GWASs) from our group and other researchers have identified a collection of common germline variants (with minor allele frequency [MAF] $\geq$ 1%) that were significantly associated with HCC risk.[2–8] These HCC-associated variants affected several genes, such as *kinesin family member 1B* (*KIF1B*)[7] and well-known DNA repair genes *X-ray repair cross complementing protein 1* and *3* (*XRCC1* and *XRCC3*).[9,10] However, these common variants explained only a small fraction of the heritability for HCC risk.[11] It is believed that rare variants (with MAF <1%) may contribute to the ''missing heritability'' of complex diseases.[11] However, the relevance of rare variants in HCC remains largely uncharacterized.

Rare variants in double-strand DNA break (DSB) repair genes are associated with susceptibility and treatment of multiple cancers.[12] Non-homologous end-joining (NHEJ) and homologous recombination (HR) are the two major DSB repair pathways, and the balance between them is crucial for maintaining the genome stability.[13] Given that poly(ADP-ribose) polymerase (PARP) inhibition causes synthetic lethality in tumors with defects in HR repair,[14] alterations in HR repair pathway were specifically exploited for targeted therapy against cancers. A prime example of such a tailored approach is the application of PARP inhibitors (PARPi) in the treatment of ovarian and breast cancer patients with *BRCA1/2* mutations.[15] Recently, several clinical studies have expanded PARPi to prostate and pancreatic cancers with HR repair deficiency.[16] In fact, PARPi is also considered to be a promising treatment strategy for HCC in recent years.[17] For example, it has been reported that the PARPi olaparib could overcome sorafenib resistance and improve the therapeutic efficacy of current sorafenib therapy.[18] Besides, the combination of PARPi olaparib with DNA-dependent protein kinase inhibitor NU7441 was demonstrated to be a potential therapy for HCC.[19] Therefore, identifying HR repair deficiency (referred to as ''BRCAness phenotype'') in cancer patients, including HCC patients, has become a promising strategy for precision therapy using PARPi.[16]

Here, we performed a rare-variant association study (RVAS) for HCC in Chinese populations and identified a collection of novel HCC-associated rare variants and genes, including the *nuclear RNAi-defective 2* (*NRDE2*) gene and its rare variant p.N377I. NRDE2 suppresses HCC through promoting HR-mediated DNA repair, while its variant p.N377I confers a loss-of-function effect and sensitizes the HCC cells to PARPi. This study highlights the contribution of rare variants in HCC susceptibility and presents a promising therapy strategy for HCC patients.

RESULTS

RVAS of HCC

To identify the rare variants conferring genetic susceptibility to HCC, we performed a two-stage RVAS (Figure S1A). In the discovery stage, 361 HCC patients (cases) and 1,757 cancer-free subjects (controls) from southern China were subject to high-throughput DNA sequencing (Tables S1 and S2; Figures S1B and S1C). After quality controls, we retained 348 cases and 1,749 controls, and detected a total of 172,206 nonsynonymous single nucleotide variants (SNVs) and 14,725 insertions or deletions (indels) (Table S3). Among these variants, a total of 142,547 SNVs/indels were defined as rare variants (with MAF <1%), which were then used in RVAS by two strategies: single-variant-based and gene-based analyses, respectively.

In the single-variant-based analyses, a total of fourteen SNVs showed suggestive associations with HCC risk ($p < 1.0 \times 10^{-5}$, Fisher's exact test; Figure S2A; Table S4). We then genotyped these 14 SNVs in three independent Chinese case-control populations (replication stages Ia, Ib, and II), totally consisting of 2,389 cases and 2,396 controls (Table S5). After meta-analyses for the discovery and replication stages, two SNVs reached the exome-wide threshold of $p = 5.0 \times 10^{-8}$ (rs199890497 in *NRDE2*: $p = 1.19 \times 10^{-9}$, odds ratio [OR] = 15.26; and rs139981430 in *RANBP17*: $p = 2.96 \times 10^{-8}$, OR = 10.70) (Figures 1A and S2B).

We also investigated the hypothesis that rare variants within a gene could collectively contribute to the risk of common diseases (STAR Methods). A total of eight genes reached exome-wide significance at threshold of $p = 1.0 \times 10^{-6}$ (Figures S2C–S2F; Table S6). We then performed target sequencing on these eight genes in replication stage Ia and Ib. After combined-analysis, two genes finally showed significant associations at exome-wide level, with $p = 5.20 \times 10^{-12}$ for *RTEL1* and $p = 3.11 \times 10^{-8}$ for *STEAP3*, respectively (Table S6).

We identified a total of four HCC-associated genes by single-variant-based and gene-based analyses, including *NRDE2*, *RANBP17*, *RTEL1*, and *STEAP3*. RTEL1 has been reported to act as a negative regulator of HR-mediated DNA repair, and to induce liver cancer in mice models.[20] The other three candidates have never been reported previously to be involved in the development of HCC. However, STEAP3 may act downstream of p53, mediating cell apoptosis and cell cycle progression.[21] *RANBP17* encodes a member of the importin-beta superfamily of nuclear transport receptors.[22] NRDE2 was shown to be a nuclear exosome negative regulator, which could regulate RNA interference-mediated gene silencing.[23,24] Intriguingly, the losses of copy-number aberration of *NRDE2* have been shown to confer potential prognostic relevance for clinical outcomes in melanoma.[25] We then performed high-content functional screen assays, and observed that knockdown of *NRDE2*, *RANBP17*, or *STEAP3* significantly induces HepG2 and Huh-7 cell growth and/or migration, suggesting their tumor suppressive roles in the development of HCC (Figure S3). Taken together, these data indicate the biological plausibility of these four candidate HCC-associated genes in the risk of HCC.

CellPress
OPEN ACCESS

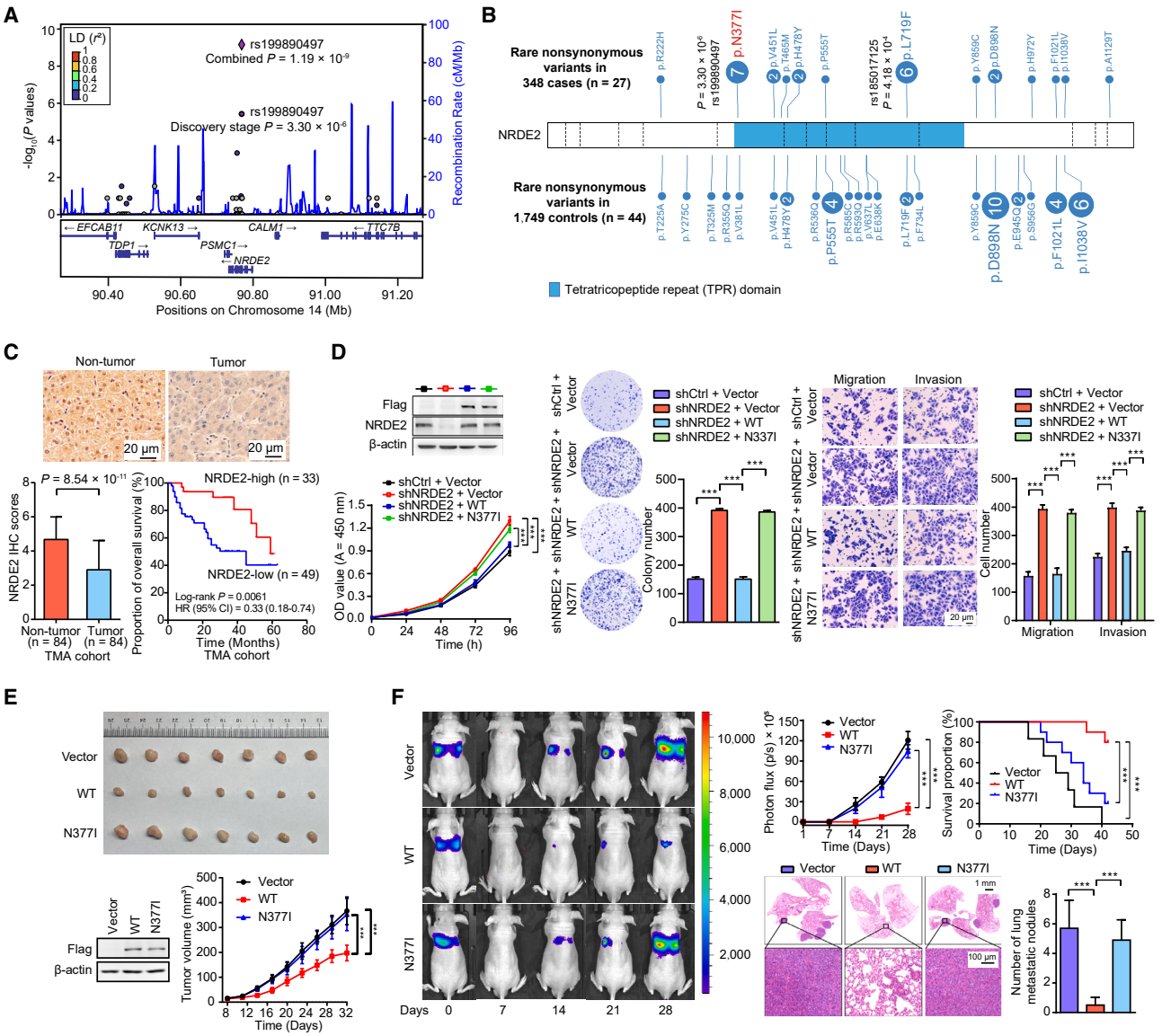

Figure 1. The rare variant rs199890497 (p.N377I) in *NRDE2* is significantly associated with HCC risk and disrupts the tumor suppressive role of *NRDE2*

(A) The regional association plot for the risk locus surrounding the index rs199890497 (p.N377I) in *NRDE2* in the discovery stage. cM, centi Morgan; LD, linkage disequilibrium.

(B) Schematic diagram of the rare nonsynonymous variants (with MAF <1%) in *NRDE2*. MAF, minor allele frequency.

(C) The NRDE2 protein expressions in HCC tissues (Tumor) are significantly lower than those in paired adjacent non-tumor liver tissues (Non-tumor) in tumor microarray (TMA) cohort (n = 84), and lower NRDE2 levels are significantly correlated with decreased overall survival rates of HCC patients. IHC, immunohistochemistry.

(D) The promoting effects of stable *NRDE2* knockdown on HepG2 cells growth/plate colony formation/migration/invasion were abolished by transiently re-expressing NRDE2 wild-type (NRDE2-WT), but not mutant NRDE2 p.N377I (NRDE2-N377I). OD, optical density.

(E) The effects of the enforced expression of NRDE2-WT or NRDE2-N377I in Huh-7 cells on subcutaneous tumor growth in BALB/c nude mice (n = 7/group). The Huh-7 cells stably transfected with Vector, NRDE2-WT, or NRDE2-N377I (1×10^6 cells diluted in 100 μL PBS) were grafted subcutaneously in the left side of the mice back.

(F) Measurement of metastases in mice injected with Huh-7 cells with enforced expression of NRDE2 (NRDE2-WT or NRDE2-N377I) via the tail veins (n = 7/group). The Huh-7 cells stably transfected with Vector, NRDE2-WT, or NRDE2-N377I (1×10^6 cells diluted in 250 μL PBS) were injected into the tail vein of the mice. The mice were monitored once a week using bioluminescence imaging. The data are shown as the mean ± standard error of mean (SEM) of three independent experiments and each experiment was done in triplicate except where noted otherwise. *$p < 0.05$, **$p < 0.01$ and ***$p < 0.001$ by two-tailed unpaired Student's t test except where noted otherwise.

Table 1. Association results for the rs199890497 and rs139981430 in the single-variant-based association analyses

Rare variants	Populations	Cases[a]	Controls[a]	ORs (95% CIs)	*p* values
rs199890497	Discovery stage (Southern China population)	341/7/0	1,749/0/0	Inf (7.34-Inf)	3.30×10^{-6}
	Replication stage Ia (Shanghai population)	667/4/0	760/0/0	Inf (0.75-Inf)	0.048
	Replication stage Ib (Guangxi population)	773/12/0	731/3/0	3.78 (1.01–20.95)	0.036
	Replication stage II (Shanxi population)	909/7/0	865/0/0	Inf (1.37-Inf)	0.016
	Total[b]			15.26 (4.74–78.18)	1.19×10^{-9}
rs139981430	Discovery stage (Southern China population)	340/8/0	1,749/0/0	Inf (8.72-Inf)	5.27×10^{-7}
	Replication stage Ia (Shanghai population)	665/7/0	755/1/0	7.94 (1.02–358.05)	0.030
	Replication stage Ib (Guangxi population)	786/4/0	744/2/0	1.89 (0.27–20.98)	0.69
	Replication stage II (Shanxi population)	914/9/0	872/0/0	Inf (1.88-Inf)	0.0040
	Total[b]			10.70 (3.74–42.04)	2.96×10^{-8}

CI, confidence interval; Inf, Infinity; OR, odds ratio.
[a]Counts of TT/TA/AA genotypes for rs199890497 and TT/TC/CC genotypes for rs139981430, respectively.
[b]Combined analyses of data generated from all of the stages were conducted to assess the pooled genetic effects. ORs were calculated on the basis of the rs199890497 A and rs139981430 C allele, respectively.

NRDE2 suppresses HCC and its rare variant p.N377I confers loss-of-function effects

The rs199890497 in *NRDE2* (p.N377I) was the top association signal in the single-variant-based analyses, with 1.1% cases (30 of 2,737) and 0.07% controls (3 of 4,145) harboring the risk A allele ($p = 1.19 \times 10^{-9}$; Figures 1A and 1B; Table 1). The cases with rs199890497-A allele are younger than the other cases (mean age, 42.8 vs. 49.6 years old, $p = 0.0012$; unpaired t test). No significant sex-specific or cirrhosis-specific effect at rs199890497 was observed ($p = 0.93$ and 0.43, respectively; χ^2 test). The rs199890497-A allele was observed in 2.1% (3 of 143) and 1.3% (2 of 160) of the HCC cases in another Chinese HCC cohort and an Asian HCC cohort from The Cancer Genome Atlas Program (TCGA) database, and in multiple non-tumor Chinese cohorts with frequencies of 0.13%–0.23% (Table S7). Notably, *NRDE2* also showed a significant association signal in the gene-based analysis, with ~2.4% of cases (43 of 1,814) and ~0.5% of controls (15 of 3,259) carrying rare deleterious *NRDE2* variants ($p = 2.62 \times 10^{-9}$; Table S6). These findings therefore indicate the robustness of the association signal of *NRDE2* in HCC risk.

Further, NRDE2 protein expressions were significantly lower in HCC tissues than in adjacent non-tumor liver tissues from a collection of 84 HCC patients (TMA cohort), and the low NRDE2 expressions in HCC tissues predicted a significantly decreased overall survival (OS) rate (Figure 1C; Table S8). Next, we collected a proteomic dataset (CHCC-HBV, including 159 paired HCC tissues and adjacent non-tumor liver tissues)[26] and two transcriptomic datasets (TCGA-LIHC, including 351 HCC tissues and 49 adjacent non-tumor liver tissues; and GEO: GSE76427, including 115 HCC tissues and 52 adjacent non-tumor liver tissues). Consistently, we observed that NRDE2 expression levels are significantly lower in HCC tissues than in adjacent non-tumor liver tissues in these datasets (all $p < 0.05$, Mann-Whitney *U* test; Figure S4A). Further, the low NRDE2 levels in HCC tissues were associated with a significantly decreased OS rate (Figure S4A). Moreover, pan-cancer analyses based on TCGA datasets showed that *NRDE2* mRNA levels are significantly lower in tumor tissues compared with adjacent non-tumor tissues, and the low *NRDE2* levels predict decreased OS rate in several other types of cancer, including breast cancer and kidney cancer (all $p < 0.05$, Mann-Whitney *U* test; Figure S4B). Intriguingly, lower *NRDE2* mRNA levels were also significantly correlated with increased HCC metastases (GEO: GSE63018, including 10 primary HCC tissues and 16 metastasis tissues, $p = 1.3 \times 10^{-3}$; and GEO: GSE364, including 13 primary HCC tissues without metastasis and 26 primary HCC tissues with metastasis, $p = 0.015$, Mann-Whitney *U* test; Figure S4C). Together, the datasets derived from distinct entities suggest that the low *NRDE2* expressions predict poor clinical outcome.

We then assessed the functional relevance of *NRDE2* and its rare variant p.N377I (NRDE2-N377I) in HepG2 and Huh-7 cells, which were validated to be wild-type (WT) for *NRDE2*. We observed that *NRDE2* significantly suppresses the cell growth, plate colony formation, migration, and invasion in HepG2 and Huh-7 cells (Figures S4D–S4I; Table S5), whereas NRDE2-N377I does not affect NRDE2 protein expression but disrupts these inhibitory effects (Figures S4G–S4I). Moreover, the tumor-promoting effects of *NRDE2* knockdown could be completely abolished by enforced expression of NRDE2-WT, but not by the enforced expression of NRDE2-N377I (Figures 1D and S4J). Consistent with *in vitro* results, *NRDE2* could significantly reduce the subcutaneous tumor growth and tumor metastasis of Huh-7 cells (Figures 1E, 1F, and S4K–S4M), whereas NRDE2-N377I abolished these inhibitory effects (Figures 1E, 1F, S4L, and S4M). Taken together, these observations indicate that NRDE2 acts as a tumor suppressor in the development of HCC, and its rare variant p.N377I exhibits a loss-of-function effect.

NRDE2 promotes HR-mediated DSB repair

To explore the underlying mechanisms by which NRDE2 suppresses HCC, we performed RNA sequencing on Huh-7 cells transfected with empty vector, wild-type NRDE2 (NRDE2-WT) and NRDE2-N377I. Both gene set enrichment analyses (GSEA)[27] and Metascape analyses showed that multiple DNA damage response (DDR)-related pathways in NRDE2-WT cells are significantly activated compared with the empty vector cells

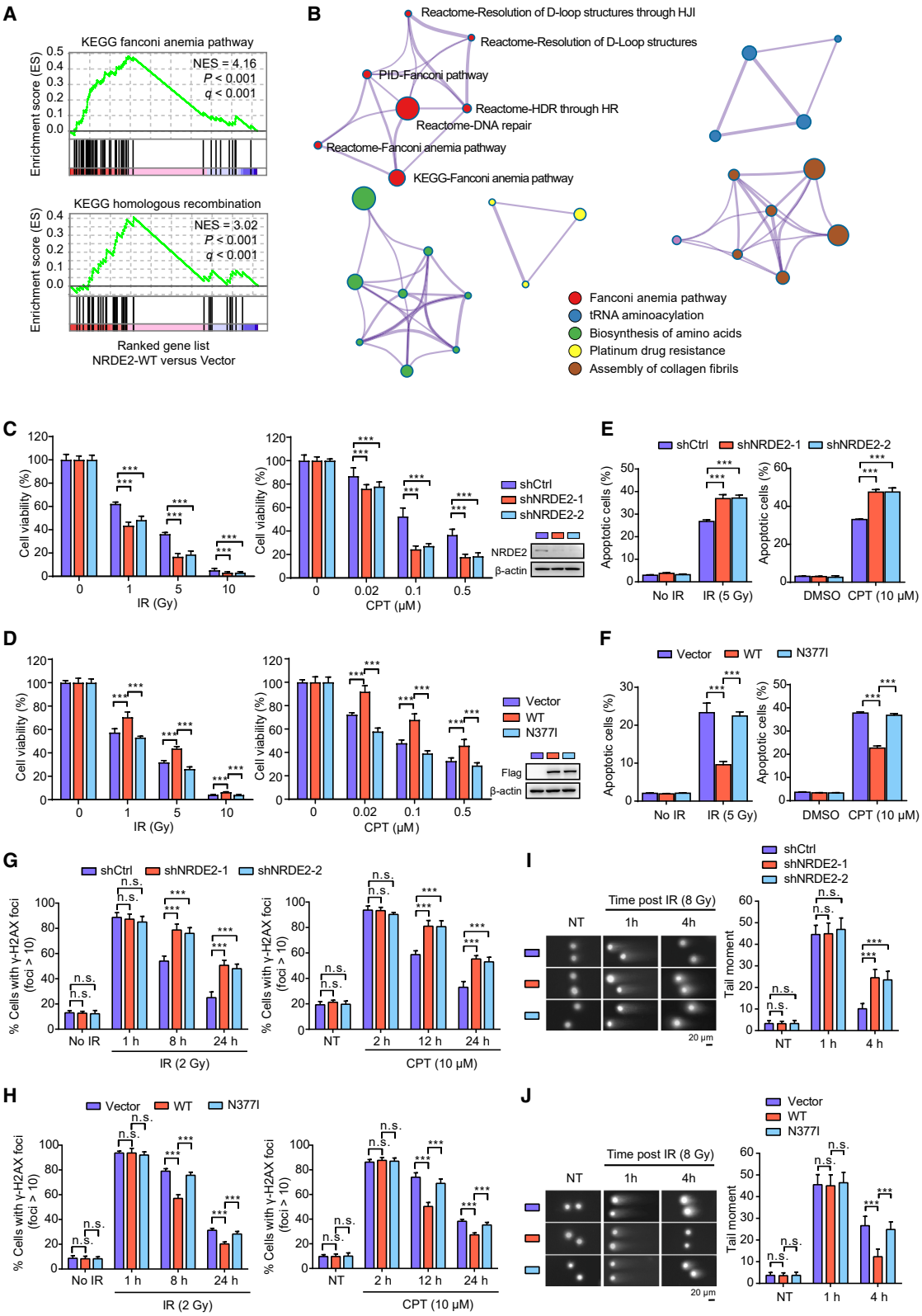

(legend on next page)

or NRDE2-N377I cells (Figures 2A, 2B, S5A, and S5B; Table S9). Thus, we hypothesize that NRDE2 plays a role in DDR. To this end, we first examined the effects of NRDE2 on response to genotoxic stresses in HCC cells. HepG2 and Huh-7 cells were treated with gradually increasing doses of ionizing radiation (IR) or increasing concentrations of camptothecin (CPT), and sensitivity to IR or CPT was assessed through clonogenic survival assays. We observed that HepG2 and Huh-7 cells with *NRDE2* knockdown formed significantly fewer clones in response to IR or CPT than control cells (Figure 2C, S5C, and S5D). On the contrary, HepG2 and Huh-7 cells transfected with NRDE2-WT, but not NRDE2-N377I, formed significantly more clones than empty vector cells (Figures 2D and S5E). These results suggest that NRDE2 reduces the sensitivity of HepG2 and Huh-7 cells to IR or CPT, whereas NRDE2-N377I abolished this effect. Moreover, when cells were treated with IR or CPT, NRDE2 could decrease the cell apoptosis, whereas NRDE2-N377I abolished this inhibitory effect (Figures 2E, 2F, S5F, and S5G). These results suggest that NRDE2 plays a role in response to DNA damage, and NRDE2-N377I confers loss-of-function effects.

Next, we investigated whether NRDE2 affects the DNA repair in HCC cells. We observed that in response to IR or CPT, *NRDE2* knockdown significantly delays the clearance of γ-H2AX foci in HepG2 and Huh-7 cells (Figures 2G and S6A–S6C). Conversely, enforced expression of NRDE2-WT significantly accelerated clearance of γ-H2AX foci in HepG2 and Huh-7 cells, while NRDE2-N377I abolished this effect (Figures 2H and S6D–S6F). The neutral comet assays also revealed a substantial DSB repair defect in *NRDE2*-knocked-down HepG2 and Huh-7 cells at 4 h after treatment with IR (Figures 2I and S6G). On the contrary, the cells with enforced expression of NRDE2-WT revealed a markedly increased DNA repair capacity, while enforced expression of NRDE2-N377I abolished this effect (Figures 2J and S6H). Moreover, the delayed tail moment effects of *NRDE2* knockdown could be completely abolished by enforced expression of NRDE2-WT, but not NRDE2-N377I (Figures S6I and S6J). We further confirmed a significant negative correlation between the protein levels of NRDE2 and γ-H2AX in HCC tissues from the TMA cohort (Figure S6K). Together, these results suggest that NRDE2 is a positive regulator of DDR.

We then asked whether NRDE2 relocates to the sites of DNA lesions. First, we observed that the nuclear foci of endogenous NRDE2, which were mostly co-localized with γ-H2AX, are readily detected in HCC cell lines HepG2 and Huh-7 after IR or CPT treatment (Pearson's correlation coefficient $r = 0.915–0.930$; Figure 3A, 3B, S7A, and S7B). Notably, we also observed that not all NRDE2 foci co-localized with γ-H2AX (Figures 3A, 3B, S7A, and S7B), indicating the possibility of other functions of NRDE2. Similar results were observed in U2OS cells (a well-established cell model in DDR studies) after IR or CPT treatment (Figures S7A and S7B). To further characterize the kinetics of this NRDE2 recruitment, we induced the enforced expression of GFP-NRDE2-WT or GFP-NRDE2-N377I in U2OS cells. As expected, a fraction of NRDE2-WT was efficiently recruited to sites of DNA damage induced by laser micro-irradiation within 2 min, while NRDE2-N377I displayed lower affinity to DNA damage sites than NRDE2-WT (Figure 3C). The chromatin immunoprecipitation assays further demonstrated that NRDE2 is recruited to the site-specific DSBs that are generated by I-SceI meganuclease (Figure 3D). Together, these findings suggest that NRDE2 is directly involved in DSB repair by relocating to the sites of DNA lesions.

NHEJ and HR are the two major DSB repair pathways in mammalian cells.[28] We then investigated which DNA repair pathways might be regulated by NRDE2. To this end, we used the DR-GFP and EJ5-GFP reporter assays in U2OS and HEK293T cells, which are widely used in DDR research.[29] We found that *NRDE2* knockdown significantly reduces the HR efficiency; conversely, the enforced expression of NRDE2-WT significantly induces it, whereas the enforced expression of NRDE2-N377I had no detectable effect (Figures 3E, 3F, S7C, and S7D). However, NRDE2 had no apparent effect on NHEJ efficiency (Figures 3E, 3F, S7C, and S7D). Similar results were observed in HCC cell lines HepG2 and Huh-7 (Figures S7C and S7D). Next, we examined the effect of NRDE2 on the recruitments of RPA2 and RAD51, two critical HR factors,[30] to DNA damage sites by monitoring their foci formation using immunofluorescence analyses. In line with the promotion role of NRDE2 in HR repair, *NRDE2* knockdown significantly suppressed the recruitments of RPA2 and RAD51 to DNA damage sites upon IR treatment in HepG2 and Huh-7 cells (Figures 3G and S7E); conversely, enforced expression of NRDE2-WT significantly

Figure 2. NRDE2 involves in DNA damage response and promotes DNA double-strand break (DSB) repair

(A) Gene set enrichment analysis (GSEA) plot based on RNA sequencing data from the Huh-7 cells stably transfected with Vector or NRDE2-WT. NES, normalized enrichment score.

(B) The enrichment maps of Metascape results based on the significantly differentially expressed genes (NRDE2-WT vs. Vector) in Huh-7 cells.

(C and D) The effects of knockdown (C) or enforced expression (D) of NRDE2 on the sensitivities of the HepG2 cells to ionizing radiation (IR) or camptothecin (CPT; for 12 h) using clonogenic survival assays. The cell survival rates are counted by calculating the colony numbers. HepG2 cells were stably transfected with non-targeting scrambled shRNA controls (shCtrl) or NRDE2-specific shRNAs (shNRDE2-1 or shNRDE2-2), or stably transfected with Vector, Flag-NRDE2-WT (WT) or Flag-tagged-NRDE2 p.N377I (N377I). WT, wild-type.

(E and F) The effects of stable knockdown (E) or stably enforced expression (F) of NRDE2 on apoptosis in HepG2 cells in response to IR (5 Gy) or CPT (10 μM, 12 h). DMSO, dimethyl sulfoxide.

(G and H) The effects of stable knockdown (G) or stably enforced expression (H) of *NRDE2* on γ-H2AX foci formation in HepG2 cells in response to IR (2 Gy) or CPT (10 μM). NT, no treatment. The γ-H2AX foci of cells in response to IR or CPT are determined using the immunofluorescence assays.

(I and J) The neutral comet assays show that the double-strand break (DSB) repair capability is reduced in *NRDE2*-stably knocked-down (I), or induced in NRDE2-stably enforced-expressed (J) HepG2 cells. HepG2 cells are harvested at the indicated time (NT, and 1 h and 4 h post-treatment) upon IR treatment (8 Gy). The tail moment was analyzed using the CometScore software. The data are shown as the mean ± standard error of mean (SEM) of three independent experiments. n.s., not significant. $^{*}p < 0.05$, $^{**}p < 0.01$, and $^{***}p < 0.001$ by two-tailed unpaired Student's t test except where noted otherwise.

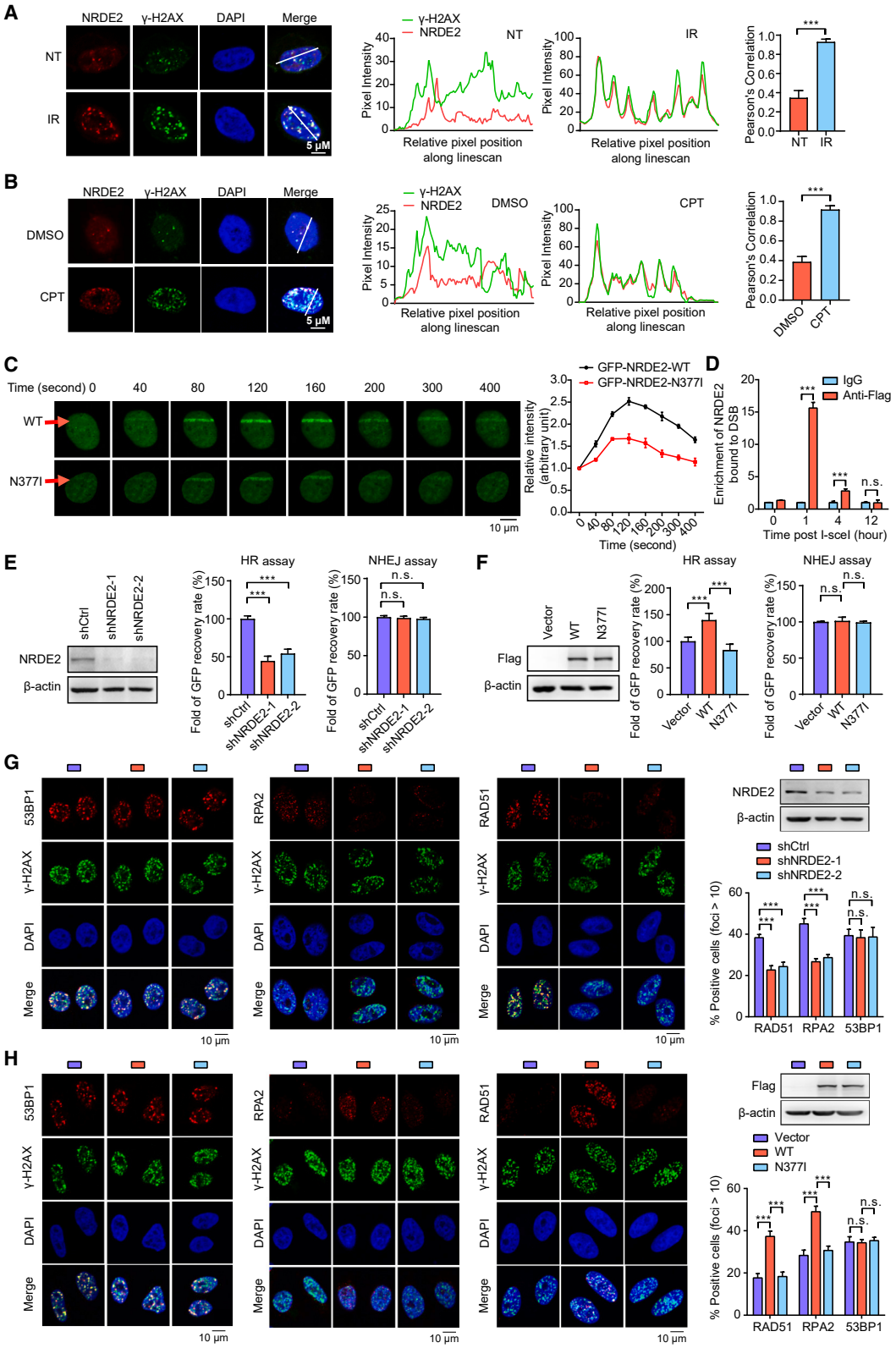

(legend on next page)

enhanced the recruitments of RPA2 and RAD51 to DNA damage sites in these cells after IR exposure (Figures 3H and S7F). However, either knockdown or enforced expression of NRDE2 did not affect the 53BP1 foci, a critical indicator of NHEJ activity (Figures 3G, 3H, S7E, and S7F).[31] Accordingly, NRDE2-N377I had no apparent effect on the recruitments of these indicators (Figures 3H and S7F). Finally, we observed that in 159 Chinese HCCs from a previous study,[26] the prevalence of the Catalog Of Somatic Mutations In Cancer (COSMIC) signature 3, which was known to be associated with failure of HR-mediated DSB repair,[32] is significantly higher in patients with lower *NRDE2* expressions (Figure S7G), suggesting the low *NRDE2* expressions predict the functional HR deficiency. Together, these results suggest that NRDE2 may specifically regulate the HR pathway, and NRDE2-N377I confers loss-of-function effects.

NRDE2 directly binds with casein kinase 2

Next, we sought to scrutinize how NRDE2 promotes HR-mediated DNA repair. Using immunoprecipitation-mass spectrometry (IP-MS) assays in HEK293T cells, we revealed that several abundant proteins associated with NRDE2 are the members of casein kinase 2 (CK2) (Figure 4A; Table S10). CK2, which is a serine/threonine-selective protein kinase composed of two closely related catalytic isoforms (CK2A1 [α] or CK2A2 [α']) that both display catalytic activity in the presence or absence of its regulatory subunit CK2B (β), is implicated in DNA repair.[33] Indeed, co-immunoprecipitation (co-IP) assays in HepG2 cells showed that NRDE2 interacts with the endogenous CK2A1/CK2A2/CK2B (Figure 4B), which was further confirmed by GST pull-down assays (Figures 4C and S8A). Immunofluorescence assays also demonstrated the co-localization of NRDE2 with these three CK2 components in nucleus of HepG2 cells (r = 0.769–0.845; Figures 4D, S8B, and S8C).[34] We then examined whether NRDE2 promotes HR repair in a CK2-dependent manner. Indeed, in response to IR, the siRNAs targeting *CK2A1*, *CK2A2*, or *CK2B* or CK2 inhibitor silmitasertib abolished the elevated HR repair efficiency by enforced expression of NRDE2-WT (Figures S8D and S8E).

To further determine the effects of p.N377I on NRDE2, we analyzed *in silico* the structure of NRDE2 protein. Multiple-species sequence alignment analyses revealed that p.N377I is highly conserved in vertebrates (Figure S9A). Three-dimensional structure simulation suggested that p.N377I decreases the molecular flexibility (Figure S9B), which might lead to the conformation change of the tetratricopeptide repeat (TPR) domain in NRDE2, where p.N377I is located. Given that the TPR domain typically serves as a protein-protein interaction module in TPR-containing proteins,[35] we first hypothesized that TPR domain of NRDE2 is required for its interaction with CK2. Indeed, co-IP assays with a series of NRDE2 deletion mutants showed that NRDE2 interacts with CK2 subunits largely via its TPR domain (Figure S9C), which was further confirmed by GST pull-down assays (Figure S9D). Moreover, in line with the *in silico* analyses, the NRDE2-N377I mutant exhibited an attenuated binding to CK2A1, CK2A2, and CK2B, compared with NRDE2-WT (Figures S9E and S9F).

Notably, NRDE2 has been reported previously to negatively regulate exosome functions by interacting with MTR4,[24] which ranked the first in our IP-MS list (Figure 4A). However, the NRDE2-MTR4 interaction was not affected by NRDE2-N377I in HCC cells (Figure S9G), indicating that the roles of NRDE2 and NRDE2-N377I in HR repair might be MTR4-independent.

NRDE2 facilitates the assembly and activity of CK2 holoenzyme

We returned to ask how NRDE2 exerts its effects through CK2. Given that the TPR-containing proteins usually act as scaffolds for the assembly of multiprotein complexes,[35] we hypothesized that NRDE2 might affect the assembly of CK2 subunits. Indeed, co-IP and GST pull-down assays showed that enforced expression of NRDE2-WT enhances the interactions among CK2 subunits, whereas NRDE2-N377I abolishes these enhancements (Figures 4E and S9H). To further confirm this hypothesis, we used a single-cell assay to assess the co-localization of proteins at an integrated LacO array.[36–38] We observed that the NRDE2-CK2 interaction is recapitulated by a Myc-tagged LacR-NRDE2-WT fusion protein with GFP-tagged CK2A1, CK2A2 or CK2B, whereas NRDE2-N377I attenuated these interactions (Figures 4F and S9I). Further, we observed that enforced expression of NRDE2-WT, rather than NRDE2-N377I, promotes the

Figure 3. NRDE2 promotes homologous recombination (HR)-mediated double-strand break (DSB) repair

(A and B) Representative confocal images of endogenous NRDE2 and γ-H2AX in HepG2 cells treated with ionizing radiation (IR, 10 Gy; A) or camptothecin (CPT, 10 μM; B) 4 h later. Co-localization was confirmed with fluorescence-intensity profiles (middle panel). Fluorescence-intensity profiles of NRDE2 and γ-H2AX were obtained using ImageJ software (v1.8.0), along a straight line (white) crossing the nucleus of a representative cell. Histograms represent mean ± standard deviation (SD) of Pearson's correlation coefficient between NRDE2 and γ-H2AX from 20 randomly selected cells in each group (right panel). NT, no treatment; DMSO, dimethyl sulfoxide.

(C) Recruitments of the wild-type NRDE2 (NRDE2-WT) or mutant NRDE2-N377I to the DNA damage sites in U2OS cells by laser micro-irradiation assays. The live-cell imaging of the recruitments of GFP-NRDE2-WT or GFP-NRDE2-N377I to laser damage tracks was generated by laser micro-irradiation in U2OS cells at the indicated time points (seconds). Red arrows indicated the regions damaged by laser micro-irradiation. Intensity quantifications of GFP-NRDE2-WT and GFP-NRDE2-N377I accumulation at laser track sites were performed using ImageJ software (v1.8.0). The intensity values in the micro-irradiated areas were pooled from 10 independent cells and plotted at the indicated time.

(D) Chromatin immunoprecipitation assays showing the recruitment of Flag-NRDE2 to I-SceI-induced DSBs in U2OS cells at the indicated time points (h).

(E and F) The effects of knockdown (E) or enforced expression (F) of *NRDE2* on the HR or non-homologous end-joining (NHEJ) repair efficiency in U2OS cells. HR or NHEJ repair efficiencies are determined using the direct repeat green fluorescent protein (DR-GFP) reporter assays or the EJ5-GFP reporter assays, respectively.

(G and H) The effects of stable knockdown (G) or stablely enforced expression (H) of *NRDE2* on 53BP1, RPA2 or RAD51 foci formation. HepG2 cells were treated with IR (2 Gy), and were immunostained with the antibodies against 53BP1, RPA2, or RAD51 followed by Alexa Fluor 555-conjugated secondary antibody. Histogram represented the numbers of 53BP1, RPA2, or RAD51 foci per nuclei. The data are shown as the mean ± standard error of mean (SEM) of three independent experiments. n.s., not significant. ***$p < 0.001$ by two-tailed unpaired Student's t test except where noted otherwise.

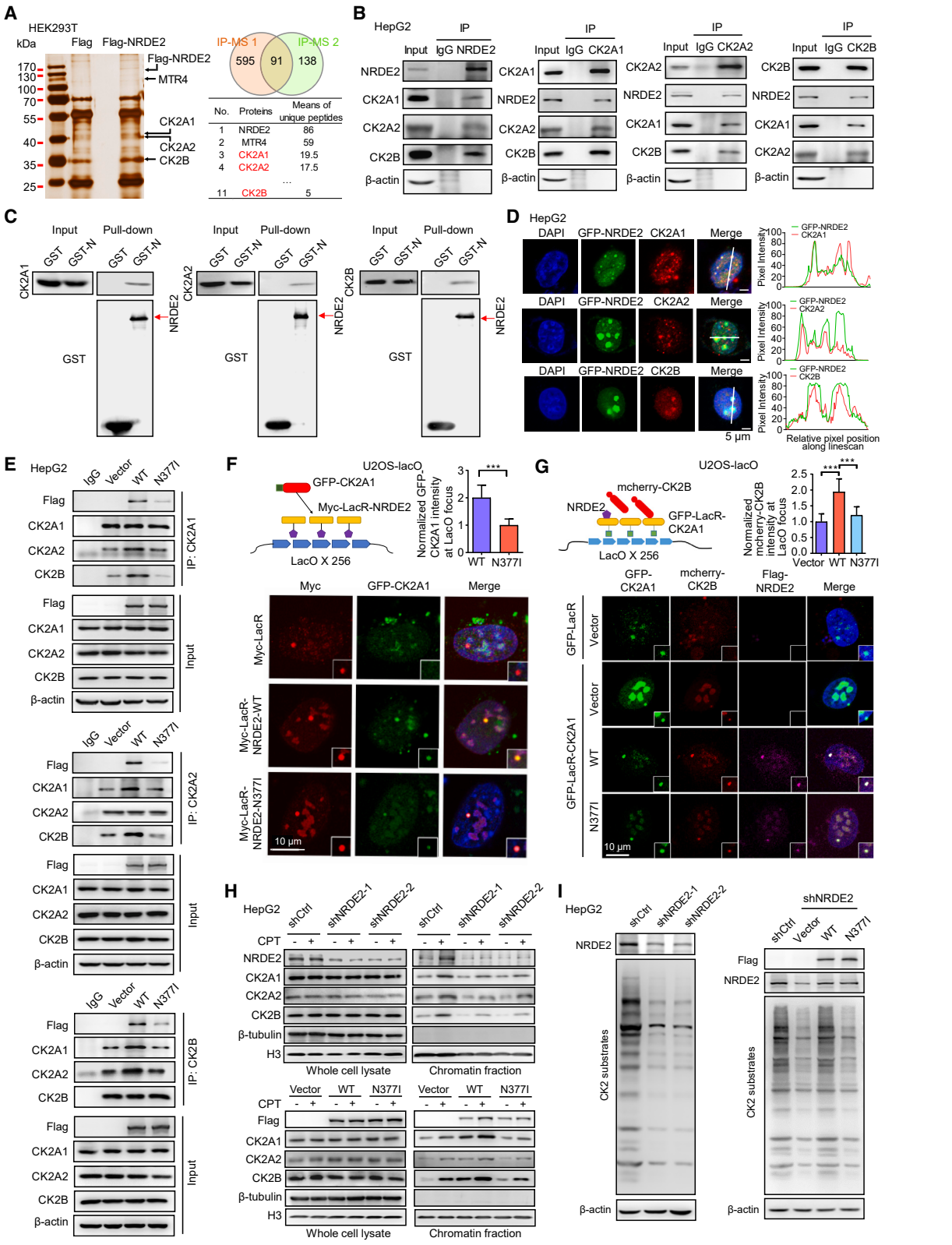

(legend on next page)

CK2 complex assembly in single-cell resolution (Figure 4G). Finally, analysis of chromatin-enriched fractions showed that CPT-induced accumulations of CK2 subunits at the chromatin are significantly decreased in *NRDE2*-knocked down HepG2 cells (Figure 4H). Conversely, enforced expression of NRDE2-WT, but not NRDE2-N377I, significantly increased these accumulations (Figure 4H). These data support the role of NRDE2 in facilitating CK2 complex assembly.

Given that CK2 deficiency impedes the DDR and renders cells hypersensitive to genotoxic agents,[39] we further hypothesized that the interaction between NRDE2 and CK2 may affect CK2 activity during the DDR. To this end, we used the phosphorylation levels of CK2 substrates as the readout of CK2 activity.[40] Indeed, we observed that the phosphorylation levels of CK2 substrates are significantly reduced by *NRDE2* knockdown (Figure 4I). Further, this reduction could be rescued by enforced expression of shRNA-resistant NRDE2-WT, but not shRNA-resistant NRDE2-N377I (Figure 4I). Together, these results suggest that NRDE2 promotes HR repair by enhancing CK2 complex assembly and its kinase activity.

NRDE2-CK2 axis induces MDC1 phosphorylation

We next attempted to identify the specific substrate(s) of the NRDE2-CK2 axis. The mass spectrometry-based phosphoproteomics assays were conducted on HEK293T cells transfected with empty vector and NRDE2-WT. A total of 456 highly confidential phosphorylation sites (with localization probability >0.75 and posterior error probability <0.001) on 378 proteins were upregulated in NRDE2-WT cells compared with control cells ($\geq$1.2-fold; Figure S10A). The kinase enrichment analyses based on these 378 proteins showed that CK2 terms are the most pronounced ones (CK2A1: false discovery rate [FDR] = 0.045, and CK2A2: FDR = 2.45×10^{-5}; Figure S10B), again confirming the role of NRDE2 in regulating CK2 activity. Further, the *in silico* motif analyses revealed that 143 of the 456 phosphorylation sites are located in the highly conserved CK2 motif p-S/T-E/D-X-E/D, corresponding to 126 proteins (i.e., the potential CK2 substrates) (Figure 5A). In addition, we obtained 763 CK2 interactors and 145 HR factors by searching the BioGRID (v4.32) and Reactome databases, respectively (Figure 5A). Finally, there are only two well-known CK2 substrates, the mediator of DNA damage checkpoint 1 (MDC1) and nucleophosmin 1 (NPM1),[41–43] which are proteins that overlap among the three candidate protein lists (Figure 5A).

Next, we demonstrated that knockdown of *MDC1*, but not *NPM1*, can abolish the elevated HR repair efficiency by enforced expression of NRDE2-WT in U2OS cells (Figures 5B and S10C). The MDC1 phosphorylation levels are reduced in *NRDE2*-or *CK2*-knocked-down HepG2 cells (Figure 5C). This reduction could be rescued by enforced expression of shRNA-resistant NRDE2-WT, but not shRNA-resistant NRDE2-N377I (Figure S10D). The co-IP assays also confirmed the interactions among MDC1, NRDE2, and CK2 subunits in HepG2 cells (Figure S10E). Downregulation of *MDC1* has been reported to be involved in tumor progression in several types of cancer.[44] However, the role of *MDC1* in HCC remains unclear. Here, we observed that knockdown of *MDC1* significantly promotes the abilities of cells growth, plate colony formation, migration and invasion of HepG2 and Huh-7 cells (Figures S10F–S10I), which could be reversed by re-expression of siRNA-resistant *MDC1* (Figures S10J–S10M). We further showed that the tumor suppressive role by enforced expression of NRDE2-WT is abolished when *MDC1* was knocked down in HepG2 and Huh-7 cells (Figures S10N–S10Q), suggesting that NRDE2 plays a tumor suppressive role in a MDC1-dependent manner. Together, these data suggest that MDC1 might be a *bona fide* substrate of CK2 in the context of NRDE2.

NRDE2-CK2 axis-mediated MDC1 phosphorylation promotes the HR repair

Next, we sought to identify the functional phosphorylation site(s) on MDC1 by NRDE2-CK2 axis. A total of four phosphorylation sites on MDC1 (S168/S329/T331/T378) detected by phosphoproteomics assays are located in the conserved CK2

Figure 4. NRDE2 interacts with CK2 complex and facilitates its assembly and activity

(A) Two independent IP-MS assays showing the associations of CK2 complex (CK2A1/CK2A2/CK2B) and NRDE2. IP assays were performed in HEK293T cells transiently overexpressing Flag-NRDE2 or empty vector. CK2, casein kinase 2; IP-MS, immunoprecipitation in combination with mass spectrometry; kDa, kilodalton.

(B) Co-immunoprecipitation (Co-IP) assays showing the interactions between NRDE2 and the components of CK2 complex (CK2A1/CKA2/CK2B) in HepG2 cells.

(C) GST pull-down assays showing the interactions between NRDE2 and CK2A1, CK2A2, and CK2B, respectively. GST-tagged wild-type NRDE2 (GST-N) was expressed and purified from *E. coli*. His-tagged CK2A1, CK2A2, and CK2B were expressed and purified from HEK293T cells.

(D) NRDE2 co-localized with CK2A1/CK2A2/CK2B at nucleus in HepG2 cells with no ionizing radiation (IR) or camptothecin (CPT) treatment by immunofluorescence assays. Fluorescence-intensity profiles were obtained using ImageJ software (v1.8.0), along a straight line (white) crossing the nucleus of a representative cell.

(E) The effects of transiently enforced expression of NRDE2-WT or NRDE2-N377I on the assembly of CK2 complex using immunoprecipitation followed by immunoblotting assays in HepG2 cells.

(F) LacO/LacR chromatin-targeting protein interaction assays showing the interactions between NRDE2-WT or NRDE2-N377I and CK2A1 in U2OS-lacO cells without IR or CPT treatment. The U2OS-lacO cells were transiently transfected with GFP-CK2A1 and Myc-LacR-NRDE2 (WT or N377I).

(G) The interactions between CK2A1 and CK2A2/CK2B assessed by LacO/LacR chromatin-targeting protein interaction assays in U2OS-lacO cells without IR or CPT treatment. The cells were transiently transfected with GFP-LacR-CK2A1, mCherry-CK2B with empty vector, Flag-NRDE2-WT, or Flag-NRDE2-N377I.

(H) The effects of endogenous NRDE2 on DNA damage induced recruitments of CK2A1/CK2A2/CK2B to chromatin in HepG2 cells treated with camptothecin (CPT, 10 μM) were investigated by chromatin fractionation assays. Western blotting assays for the total or chromatin fractions from HepG2 cells with stable knockdown of *NRDE2* or stably enforced expression of NRDE2 at 4 h after CPT treatment using the indicated antibodies.

(I) The effects of knockdown or enforced expression of NRDE2 on cellular CK2 activity in HepG2 cells. We used the phosphorylation levels of CK2 substrates as a readout of cellular CK2 activity. *NRDE2* was stably knocked down, and the NRDE2-WT and NRDE2-N377I were transiently expressed in cells. The data are shown as the mean ± standard error of mean (SEM) of three independent experiments. ***$p < 0.001$ by two-tailed unpaired Student's t test.

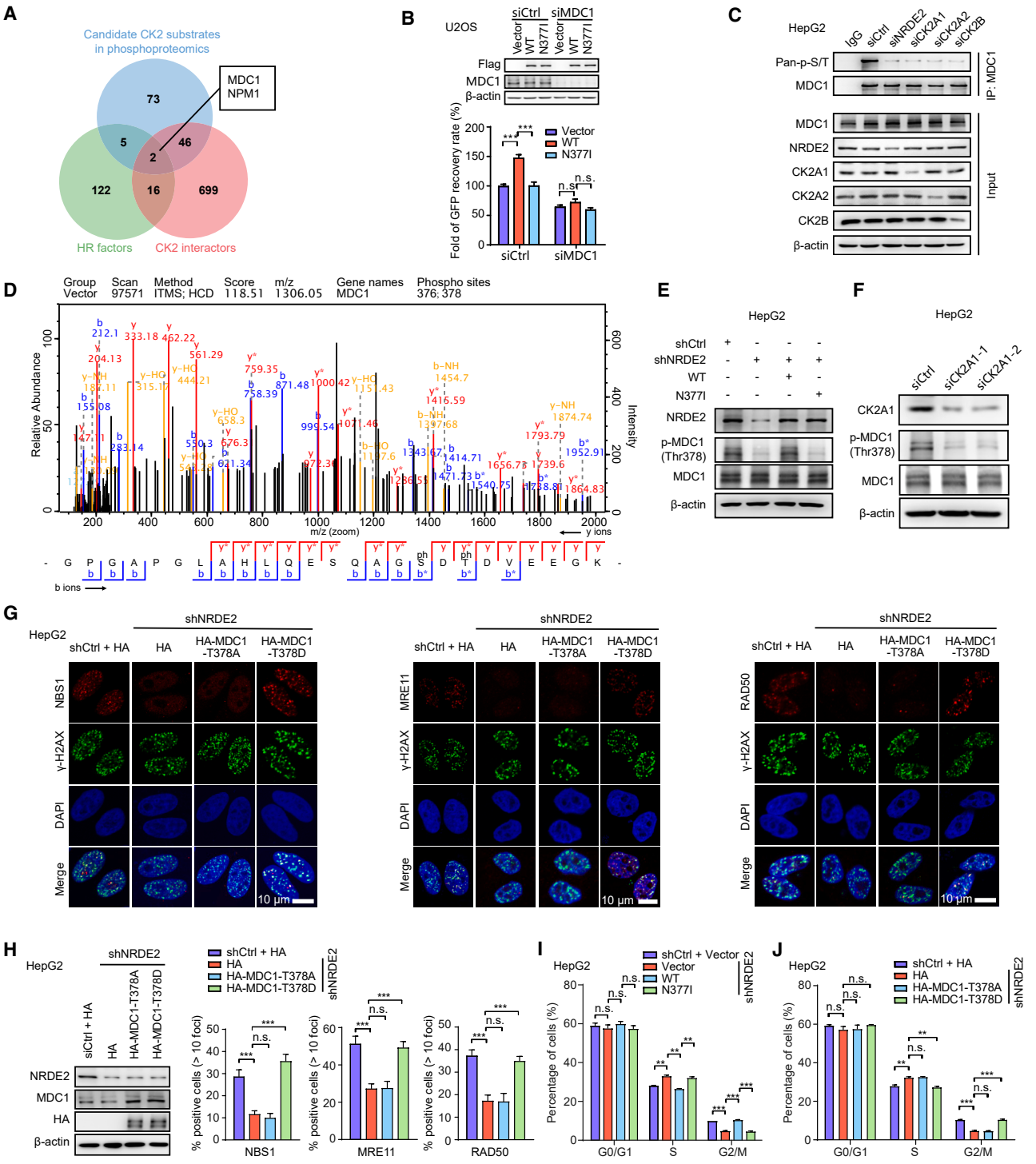

Figure 5. NRDE2-CK2 axis-mediated MDC1 phosphorylation at T378 promotes the homologous recombination (HR) repair

(A) Venn plot of candidate CK2 substrates, HR-related factors and known interactors for CK2.

(B) *MDC1* knockdown abolished NRDE2-WT-mediated enhancement of HR repair efficiency in U2OS cells. U2OS cells transiently transfected with empty vector (Vector), Flag-tagged-NRDE2-WT, or Flag-tagged-NRDE2 p.N377I (NRDE2-N377I) were transiently transfected with siCtrl or pooled MDC1-specific siRNAs.

(C) The phosphorylation of endogenous MDC1 following *NRDE2* or *CK2* transient knockdown in HepG2 cells. The MDC1 immunoprecipitates were subjected to western blotting with the anti-phosphorylated (pan-p-S/T) antibody.

(D) Selected LC-MS/MS scan of the MDC1 peptides with phosphorylated T378 and the annotated b- and y-ions.

(legend continued on next page)

motif (Figures 5D and S11A). Indeed, the phosphorylations at serine-aspartic acid-threonine (SDT) repeats of MDC1 (residues 200–420) have been reported to trigger productive interaction between MDC1 and Nibrin (NBN, also named Nijmegen breakage syndrome 1 protein [NBS1]), which in turn increases the recruitment of NBS1 to the DSB sites.[41–43] Here, we observed that in cells lacking endogenous MDC1, re-expression of phospho-deficient HA-MDC1-S329A, -T331A, or -T378A, but not HA-MDC1-S168A, fails to restore HR repair efficiency relative to cells expressing HA-MDC1-WT (Figure S11B). Further, in cells lacking endogenous NRDE2, enforced expression of phospho-deficient HA-MDC1-S329A, -T331A, or -T378A revealed less HR repair efficiency than did expression of an equivalent amount of HA-MDC1-WT (Figure S11C). However, enforced expressions of phospho-mimetic HA-MDC1-S329D, -T331D, or -T378D in cells lacking endogenous NRDE2 were able to enhance the HR repair efficiency (Figure S11C). Both phospho-deficient and phospho-mimetic mutants of MDC1 did not affect the NHEJ repair efficiency in the context of NRDE2 (Figure S11D). Collectively, these results demonstrate that the phosphorylations of MDC1 at three of the four sites (S329, T331, and T378) play essential roles for MDC1 in HR-mediated DSB repair in the context of NRDE2.

Among these three phosphorylation sites, S329 and T331 have been shown to be involved in Nijmegen breakage syndrome 1 protein (NBS1) recruitment.[41–43] Therefore, we selected T378 as a new candidate for subsequent in-depth investigation. To this end, we prepared an antibody that can specifically recognize the phosphorylated T378 on MDC1 (p-T378-MDC1). We found that NRDE2 dramatically induces the p-T378-MDC1 signal in HepG2 and Huh-7 cells, whereas NRDE2-N377I did not induce the signal (Figures S11E and S11F). Further, the p-T378-MDC1 signal disrupted by *NRDE2* knockdown could be rescued by enforced expression of shRNA-resistant NRDE2-WT, but not NRDE2-N377I (Figures 5E, S11E, and S11F). We also showed that knockdown of *CK2* efficiently reduces the p-T378-MDC1 signal, and the effect of NRDE2 on the p-T378-MDC1 signal is CK2-dependent in HepG2 and Huh-7 cells (Figures 5F and S11G–S11I). Finally, we observed a positive correlation between the protein levels of NRDE2 and p-T378-MDC1 in HCC tissues from the TMA cohort (Figure S11J). These results support that the NRDE2-CK2 axis induces the phosphorylation of MDC1 at T378.

Next, we investigated whether the NRDE2-CK2 axis-mediated MDC1 phosphorylation at T378 is required for HR repair. In response to DNA damage, the recruitment of NBS1 to DSB sites and the formation of MRE11-RAD50-NBS1 (MRN) complex are critical for the initiation of HR repair, while the recruitment of 53BP1 directs the NHEJ-mediated DNA repair.[45] In *NRDE2*-knocked-down HepG2 and Huh-7 cells under treatment with IR, we showed that enforced expression of phospho-mimetic MDC1-T378D, but not phospho-deficient MDC1-T378A, promotes the recruitment of MRE11, RAD50, and NBS1 to DSB sites (Figures 5G, 5H, S12A, and S12B). However, the recruitment of 53BP1 was not changed (Figures S12C and S12D). Additionally, we found that knockdown of *NRDE2* in HepG2 and Huh-7 cells treated with IR leads to the delayed cell cycle progression, which can be rescued by NRDE2-WT and MDC1-T378D, but not NRDE2-N377I or MDC1-T378A (Figures 5I, 5J, S13A, and S13B). Further, cell survival assays showed that *NRDE2* knockdown in HepG2 and Huh-7 cells induces a significantly increased sensitivity to hydroxyurea or ultraviolet C (UV-C) light (Figures S13C and S13D), which can be rescued by NRDE2-WT and MDC1-T378D, but not NRDE2-N377I or MDC1-T378A (Figures S13C and S13D). We further found that knockdown or enforced expression of *NRDE2* in HepG2 and Huh-7 cells treated with IR do not affect the levels of γ-H2AX and four checkpoint markers (*p*-ATM, *p*-ATR, *p*-CHK1, and *p*-CHK2) (Figure S13E). As NRDE2 has been reported to be implicated in RNA processing,[23,24] we also examined the mRNA and protein levels of these checkpoint markers and found that the expression levels of these markers do not change upon *NRDE2* knockdown (Figure S13E). These results suggest that NRDE2 regulates the cell cycle progression, but this may occur in an ATR/CHK1- and ATM/CHK2-independent manner or act downstream of the main checkpoint activator ATM/ATR. Finally, we showed that in *NRDE2*-knocked-down HepG2 and Huh-7 cells, enforced expression of MDC1-T378D, but not MDC1-T378A, can abolish the promotion effects of cell growth/plate colony formation/migration/invasion by *NRDE2* knockdown (Figures S13F and S13G). Collectively, these results suggest that NRDE2 promotes HR repair and plays a tumor suppressive role by enhancing CK2-mediated MDC1 phosphorylation at the T378 site, whereas NRDE2-N377I impairs these functions.

(E) The inhibition effects of *NRDE2* knockdown on MDC1 phosphorylation at T378 in HepG2 cells could be abolished by NRDE2-WT, but not NRDE2-N377I. The HepG2 cells were stably transfected with shCtrl and pooled NRDE2-specific shRNAs. Then the HepG2 cells with *NRDE2* knockdown were transiently transfected with NRDE2-WT or NRDE2-N377I. The p-T378-MDC1 signal was determined using an antibody specifically recognizing the T378-MDC1 phosphorylation.

(F) The effects of knockdown of *CK2A1* on the phosphorylation at T378 of endogenous MDC1 in HepG2 cells. The HepG2 cells were transiently transfected with siCtrl or CK2A1-specific siRNAs.

(G and H) The effects of T378 phosphorylation on MDC1-mediated recruitments of the MRN complex subunits (NBS1, MRE11, and RAD50) at DSB sites in HepG2 cells treated with IR (2 Gy). Endogenous *NRDE2* was stably knocked down by shRNAs, and then the phospho-mimetic (T378D) or -deficient (T378A) mutants of MDC1 were transiently overexpressed in cells as indicated. Then, cells were treated with IR (2 Gy).

(I) The effects of NRDE2 on cell cycle progression after DNA damage in HepG2 cells treated with IR (2 Gy). Endogenous *NRDE2* was stably knocked down by shRNAs, and the shRNA-resistant NRDE2-WT or NRDE2-N377I was then transiently re-expressed in cells as indicated. Percentage of cell cycle phases was measured by 5-bromodeoxyuridine (BrdU) incorporation with the cells being treated with IR (2 Gy).

(J) The effects of NRDE2-mediated T378 phosphorylation on MDC1 induced intra-S-phase checkpoint after DNA damage in HepG2 cells treated with IR (2 Gy). Endogenous *NRDE2* was stably knocked down by shRNAs, and then the MDC1-phospho-mimetic (T378D) or -deficient (T378A) mutants of MDC1 were transiently overexpressed in cells as indicated. The data are shown as the mean ± standard error of mean (SEM) of three independent experiments. n.s., not significant. $^{**}p < 0.01$ and $^{***}p < 0.001$ by two-tailed unpaired Student's t test.

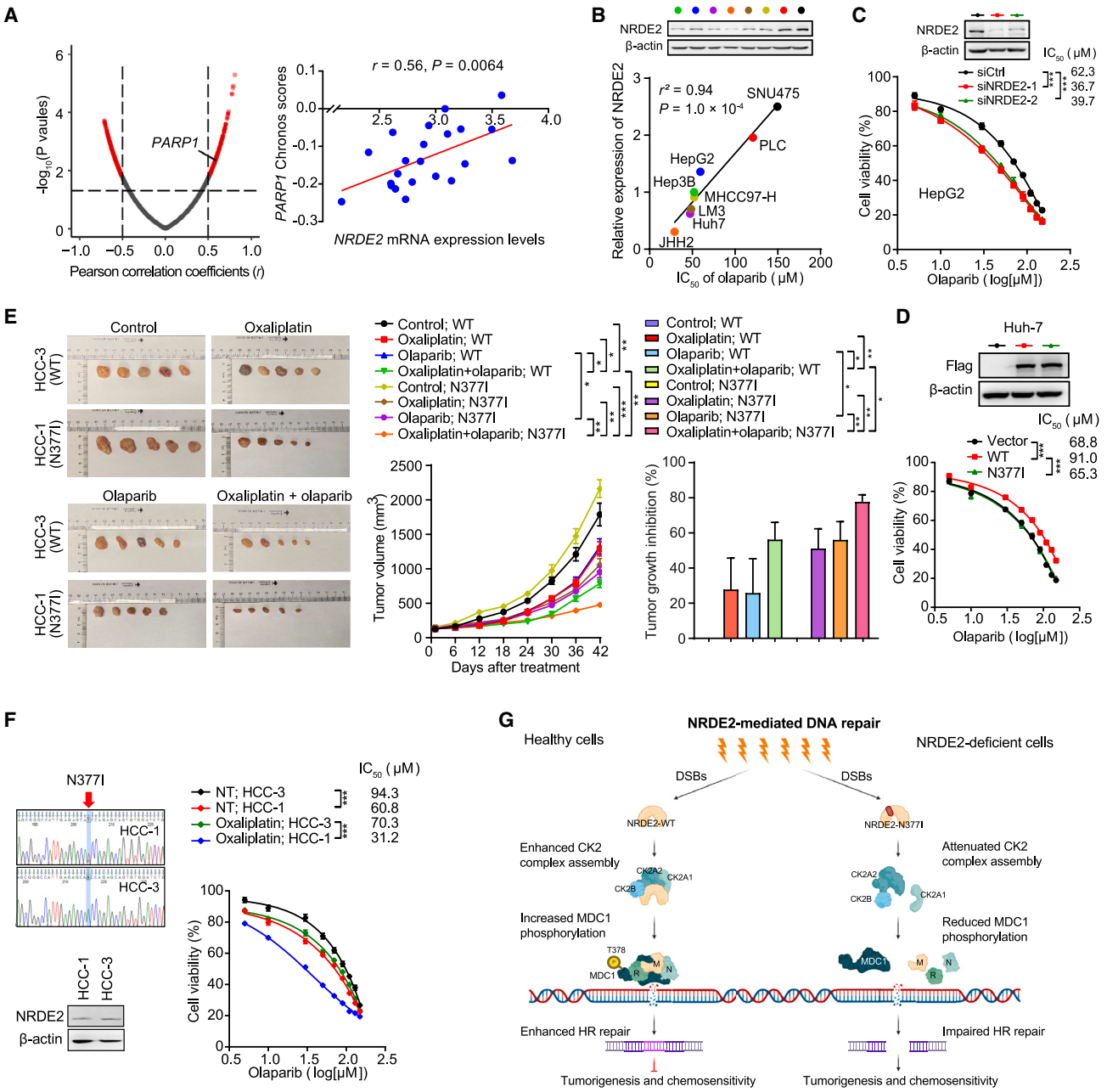

Figure 6. *NRDE2* deficiency sensitizes HCC cells to PARP1 inhibitor

(A) A positive correlation between the expression levels of *NRDE2* and *PARP1* dependency scores in liver cancer cell lines from the Dependency Map database (https://depmap.org/portal/).

(B) A negative correlation between the expression levels of *NRDE2* and sensitivity to the PARP1 inhibitor olaparib in multiple HCC cell lines. Cellular viability was assessed in eight types of HCC cell line after treatment with different doses of olaparib for 72 h by CCK-8 assays. IC_{50}, the half-maximal inhibitory concentration.

(C) Transiently knockdown of *NRDE2* enhances the sensitivity of HepG2 cells (with higher endogenous *NRDE2* levels) to the PARP1 inhibitor olaparib.

(D) Transiently enforced expression of NRDE2-WT reduces the sensitivity of Huh-7 cells (with lower endogenous *NRDE2* levels) to the PARP1 inhibitor olaparib. The percentage of cell viability in HepG2 (C) and Huh-7 (D) cells was assessed after treatment with indicated doses of olaparib for 72 h.

(E) Measurements of tumor growth inhibition rate (%TGI) and tumor volume (mm^3) in the PDX models with endogenous NRDE2-N377I (HCC-1 and HCC-2) and in the PDX models with NRDE2-WT (HCC-3 and HCC-4). The PDX models were treated with olaparib, oxaliplatin, or the combination (STAR Methods). On the 42nd day after treatment, the tumors from PDX HCC-1 and HCC-3 are shown in the left panel. The middle and right panels represent the relative tumor volume over time and the %TGI, respectively.

(F) Sensitivity of primary HCC cells (from PDX HCC-3 and HCC-1) to olaparib or the combination treatment with oxaliplatin and olaparib. Sanger sequencing showed that HCC-1 cells harbor the heterozygous NRDE2-N377I variant, and the variant allele frequency of the mutant allele was obviously higher than that of the

(legend continued on next page)

NRDE2 deficiency sensitizes HCC cells to PARPi

Given that PARPi could selectively kill tumors with defects in HR repair,[14] we then asked whether tumor cells with *NRDE2* deficiency might have increased sensitivity to PARPi. Indeed, the analyses based on the Dependency Map (DepMap) portal[46] revealed a markedly negative correlation between *NRDE2* expressions and sensitivity to DNA damage agents in cancer cells, including PARPi (Figures S14A, and S14B; Table S11). Furthermore, we found that *NRDE2* expression levels are significantly positively correlated with *PARP1* Chronos scores in 22 types of liver cancer cell lines from the DepMap database (Figure 6A), suggesting the synthetic lethal effects between *NRDE2* deficiency and PARPi in HCC cells. Then, we found there indeed exists a negative correlation between the expressions of *NRDE2* and sensitivity to PARPi olaparib in a panel of eight types of HCC cells (Figure 6B). Further, we showed that knockdown of *NRDE2* in HCC cells expressing high levels of endogenous *NRDE2* (HepG2 and SNU475 cells) significantly reduces cells olaparib resistance (Figures 6C and S14C). Conversely, enforced expression of NRDE2-WT in HCC cells expressing low levels of endogenous *NRDE2* (Huh-7 and JHH-2 cells) significantly reduced cell olaparib sensitivity; whereas the enforced expression of NRDE2-N377I did not have this effect (Figures 6D and S14C).

The effects of NRDE2 on olaparib sensitivity were further tested in HCC PDX models. We successfully established four PDX models: two of which carry the NRDE2-N377I variant (HCC-1 and HCC-2), while the other two carry the WT NRDE2 (HCC-3 and HCC-4) (Figures S14D–S14F). We then treated these four PDX models with olaparib and found that the tumors derived from HCC-1/HCC-2 exhibit significantly higher tumor growth inhibition (TGI) rate than those from HCC-3/HCC-4 (Figures 6E and S14G), suggesting the higher olaparib sensitivity for HCCs with defect in *NRDE2*. Notably, there are certain differences in the results of drug sensitivity evaluation using cell lines and PDX models, which may be because the PDX model more faithfully preserves the heterogeneity, architecture, and cell composition of tumors *in vivo*.[47]

We also assessed the effects of NRDE2 on olaparib sensitivity in cultured primary HCC cells isolated from the tumor tissues of HCC-1 (NRDE2-N377I) and HCC-3 (NRDE2-WT), respectively. We confirmed that HCC-1 cells display significantly higher olaparib sensitivity than did HCC-3 cells (Figure 6F). Consistently, we confirmed that knockdown of *NRDE2* in HCC-3 cells significantly promotes cell growth, migration, and invasion; delays the clearance of γ-H2AX foci; and suppresses the recruitments of RAD51, but not 53BP1, to DNA damage sites induced by IR (Figures S14H–S14J). On the contrary, enforced expression of NRDE2-WT in HCC-1 cells significantly suppressed cell growth, migration, and invasion; accelerated clearance of γ-H2AX foci; and enhanced the recruitments of RAD51, but not 53BP1 to DNA damage sites induced by IR; whereas enforced expression of NRDE2-N377I did not have these effects (Figures S14K–S14M). Together, these findings again support that *NRDE2* deficiency sensitizes HCC cells to PARPi.

Finally, we tested whether MDC1 and its phosphorylation at T378 site are required for the *NRDE2* deficiency-mediated PARPi sensitivity in HCC cells. In HepG2 or Huh-7 cells lacking MDC1, enforced expression of NRDE2-WT failed to confer the resistance to olaparib (Figure S15A). In HepG2 or Huh-7 cells lacking NRDE2, ectopical expression of phospho-deficient MDC1-T378A conferred an increased sensitivity to olaparib, while ectopical expression of phosphor-mimetic MDC1-T378D resulted in a decreased sensitivity to olaparib, compared to the expression of the empty vector (Figure S15B). These findings therefore provide evidence that phosphorylation of MDC1 at T378 is required for *NRDE2* deficiency-mediated PARPi sensitivity.

We also showed that the *NRDE2* deficiency-mediated PARPi sensitivity is CK2-dependent in HepG2 or Huh-7 cells (Figures S15C and S15D).

The combination of PARPi and platinum can effectively kill *NRDE2*-deficient HCC cells

The platinum-based drugs are the first-line usage drugs for HCC patients.[48] Given that platinum-based drugs are the inducers of DNA damage, which require HR repair, we postulated that platinum might facilitate HCC cell sensitivity to PARPi. We observed that knockdown of *NRDE2* in HepG2 or SNU475 cells (with high *NRDE2* expression) significantly increases the sensitivity to oxaliplatin, while enforced expression of NRDE2-WT, but not NRDE2-N377I in Huh-7 and JHH-2 cells (with low *NRDE2* levels) significantly increases cells' oxaliplatin resistance (Figure S16A). Importantly, olaparib and oxaliplatin treatment in combination revealed additional effects in reducing cell growth of all cells, and the combination effects were stronger in NRDE2-high cells with *NRDE2* knockdown than those without, and in NRDE2-low cells with enforced expression of NRDE2-N377I than those with enforced expression of NRDE2-WT (Figure S16A).

We also tested the combination effects of olaparib and oxaliplatin on cultured PDX HCC-1 (with NRDE2-N377I) and HCC-3 cells (with NRDE2-WT) isolated from PDX. Consistently, HCC-1 cells displayed higher sensitivity to olaparib than HCC-3 cells when oxaliplatin was used (Figure 6F). Meanwhile, *NRDE2* knockdown significantly enhanced HCC-3 cells' sensitivity to olaparib and oxaliplatin combination (Figure S16B). Enforced expression of NRDE2-WT significantly reduced olaparib and oxaliplatin combination sensitivity in HCC-1 cells, while the enforced expression of NRDE2-N377I did not have this effect (Figure S16B). Consistently, olaparib and oxaliplatin combination revealed significant effects on reducing tumor growth in all PDX models, and the effects were stronger in PDX HCC-1/HCC-2 than in PDX HCC-3/HCC-4 (Figures 6E and S14G). Taken together, these results suggest that, when combined with

reference allele (>2-fold), and HCC-3 cells harbor the wild-type genotype. The percentage of cell viability in primary HCC cells was assessed after treatment with these drugs for 72 h. NT, no treatment.

(G) Model of the function and underlying mechanism that NRDE2 suppresses tumorigenesis and chemosensitivity. This figure was created using BioRender.com. The data are shown as the mean ± standard error of mean (SEM) of three independent experiments. $^{*}p < 0.05$, $^{**}p < 0.01$ and $^{***}p < 0.001$ by two-tailed unpaired Student's t test.

oxaliplatin, the efficiency of PARPi treatment is substantially enhanced in tumors with *NRDE2* deficiency.

DISCUSSION

The contributions of both common and rare variants to a range of common diseases, including cancers, have been well established for decades.[11] With regard to HCC, previous GWASs have identified numerous common variants that were significantly associated with susceptibility to HCC. However, the contribution of rare variants to HCC risk was largely uncharacterized. Here, we conducted the first RVAS on the risk of HCC in a Chinese population, and successfully identified a collection of rare variants and candidate genes implicated in HCC, which made up the "missing heritability" and expanded our understanding of the genetic architecture of HCC.

We revealed that *NRDE2* is a novel regulator that promotes DNA damage repair and exerts a suppressive effect on HCC. NRDE2 was originally discovered for its roles in nuclear RNA interference in *C. elegans*.[49] After that, Nrl1 (a homologous protein of human NRDE2) in *S. pombe* was suggested to promote HR repair by suppressing R-loop formation.[50] In humans, NRDE2/MTR4 protein complex has also been suggested to be involved in DNA damage repair, but it functions in a non-R-loop formation manner, and its specific mechanism is still unclear.[51] Recently, human and mouse NRDE2 was shown to be required for RNA processing.[23,24,52] Here, we demonstrate that human NRDE2 is involved in HR-mediated DNA repair through CK2 holoenzyme-dependent MDC1 phosphorylation, therefore exhibiting a new mechanism for NRDE2 in humans. According to the revealed function of NRDE2, we postulate that knockdown of *NRDE2* might make cells more susceptible to death due to spontaneous DNA damage, which was not observed in this study. As RNA splicing plays important roles in the development of HCC,[53] we think that this observation might be due to the RNA splicing function or other unrevealed functions of NRDE2. Notably, in DR-GFP reporter assays, we observed that *NRDE2* knockdown reduces HR efficiency by ~50%, while *MDC1* knockdown only reduces HR efficiency by ~20% (Figures 3E and S11B), implying that NRDE2 might regulate HR through the MDC1-independent pathway as well. In addition, given that NRDE2 plays a conserved role in RNA processing, such as RNA splicing,[23,24,52] exploring whether NRDE2 controls HR through RNA processing is also of interest and deserves further studies.

CK2, which is one of the earliest identified protein kinases, is involved in numerous biological processes, including response to DNA damage.[54] The underlying mechanisms of regulation of CK2 activity have been extensively studied, including its subunits being regulated by other proteins, protein post-translational modification, and dimerization, etc.[54] Here, we provided evidence that NRDE2 may act as a scaffold protein and directly interacts with the subunits of CK2 holoenzyme and promotes its assembly and enzyme activity. Further, our findings establish a vivid example that NRDE2 can play important roles by affecting the ability of CK2 to phosphorylate certain substrate(s), such as DNA damage repair here. To our best knowledge, this is a novel mechanism related to the regulation of CK2 holoenzyme activity.

The synthetic lethal effect provides a promising therapeutic strategy in numerous cancers.[55] The best-known example of synthetic lethality is the interplay between HR deficiency and PARPi, which has been approved for use in multiple HR-deficient cancers, especially in cancers with *BRCA1/2* mutations.[31] However, synthetic lethal interactions remain largely undisclosed, and relatively few synthetic lethality-related drugs have been tested clinically.[15] Here, we provided evidence that deficiency in the *NRDE2* gene could result in HR dysfunction, which phenocopies the *BRCA1/2* mutations (or BRCAness).[56] Notably, we further observed that *NRDE2* deficiency sensitizes HCC cells to PARPi. Especially, PARPi-induced killing of HCC cells with *NRDE2* deficiency is synergistic with chemotherapeutic agents such as oxaliplatin, therefore providing a novel candidate biomarker for PARPi therapy in HCC. In this study, the NRDE2 TPR domain was affected by rare germline variants in ~4.4% of the cases (79 of 1,814). Besides, the loss of heterozygosity (LOH) or other somatic alterations in *NRDE2* may also result in deficiency of this gene. Interestingly, whole-genome/exome sequencing of HCC tissues from the seven HCC patients with heterozygous germline NRDE2-N377I in the discovery stage showed that three of the tumors carry homozygous NRDE2-N377I (with variant allele frequency [VAF] > 0.8), therefore indicating their locus-specific LOH. In addition to these three tumors, the VAFs of the NRDE2-N377I mutant allele in the other two tumors were higher than 0.7, suggesting the suggestive event of LOH at this locus.[57] These results are consistent with the notion that two hits of HR-related genes typically exist in certain tumors.[58] Additionally, besides *NRDE2*, three other genes in the HR pathway (*RTEL1*, *BRCA1* and *BRCA2*) also showed suggestive associations with HCC risk in this study. Thus, rare variants in these four genes totally affected approximately one-fifth of HCC patients in the discovery stage (79 of 384), who might be sensitive to PARPi and therefore benefit clinically (Figure S17A; Table S12). In addition to HCC, we observed that *NRDE2* is downregulated in several other tumors, and low *NRDE2* expressions predict poor outcomes in multiple cancers (Figure S4B). Thus, whether *NRDE2* deficiency could be a biomarker for PARPi treatment in other types of cancer certainly warrants further investigations.

In summary, this study provides new insights into the genetic mechanisms of HCC risk (Figure 6G). Given that the novel function of the NRDE2-CK2-MDC1 axis is regulating HR-mediated DNA, damaging repair, and sensitizing to PARPi, our work provides a new potential strategy for the treatment of HCC, which may lead to the development of new effective strategies for the treatment of this malignancy.

Limitations of the study

Although the population size in the discovery stage in this study was limited compared with traditional GWASs, high-throughput DNA sequencing study was pivotal for the rare variants that usually could not be discovered by traditional GWASs. Additionally, our RVAS exbibits a sufficient statistical power in 348 cases and 1,749 controls in detecting the rs199890497 at *NRDE2* gene, with an estimated power of ~86% (Figure S17B).

STAR★METHODS

Detailed methods are provided in the online version of this paper and include the following:

- KEY RESOURCES TABLE
- RESOURCE AVAILABILITY
  - Lead contact
  - Materials availability
  - Data and code availability
- EXPERIMENTAL MODEL AND SUBJECT DETAILS
  - Human subjects
  - Animal studies
  - Cell lines
- METHOD DETAILS
  - High-throughput DNA sequencing, variants calling and quality controls
  - RVAS in the discovery stage
  - Single-variant-based replication studies
  - Knockdown or enforced expression of genes
  - High-content functional screening assays
  - Publicly available transcriptome and proteome datasets analyses
  - Cells growth and plate colony formation assays
  - Cells migration and invasion assays
  - Immunoprecipitation in combination with mass spectrometry (IP-MS) assays
  - *In silico* structure prediction for NRDE2 protein
  - Chromatin tethering assays using the LacR/LacO array system
  - Phosphorylation site analysis by liquid chromatography-tandem mass spectrometry (LC-MS/MS)
  - Kinase enrichment and motif analyses
  - Patient-derived tumor xenograft (PDX) mice models studies
- QUANTIFICATION AND STATISTICAL ANALYSIS
  - The power analyses
  - Statistical analyses
- ADDITIONAL RESOURCES

SUPPLEMENTAL INFORMATION

Supplemental information can be found online at https://doi.org/10.1016/j.xgen.2024.100550.

ACKNOWLEDGMENTS

We sincerely thank Dr. Huadong Pei (at the School of Medicine and Health Science at George Washington University, Washington, DC, USA) for providing the DR-GFP cassette for HR repair assays, Dr. Jeremy Stark (at the City of Hope Comprehensive Cancer Center, Duarte, CA, USA) for providing the EJ5-GFP cassette for NHEJ repair assays, and Dr. Fangwei Wang (at the Life Sciences Institute of Zhejiang University, Hangzhou City, China) for providing the LacR/LacO system. We also thank all the patients and/or their guardians for participating in this study. This work was supported by grants from the Chinese Key Project for Infectious Diseases (no. 2018ZX10302202 and 2017ZX10203205), the National Natural Science Foundation of China (no. 82273080 and 82273523), and the Open Project Program of the State Key Laboratory of Proteomics (SKLP-O201510).

AUTHOR CONTRIBUTIONS

G.Z. was the principal investigator who conceived the study and obtained financial support. G.Z., F.H., Y. Li, X. Zhang, Y.W., and X.L. designed the study. Q.S., Y. Le, J.X., Hongxing Zhang, J.A., W.J., and L.K. were responsible for the recruitment of HCC patients. X. Zuo and X. Zhang were responsible for the recruitment of control individuals. X. Liu, Q.L., C.W, H.C., J.Y., H.X., and T.W. helped to prepare the blood and tissue samples of HCC patients. Y.W., Y. Li, X. Zuo, X. Zhang, Hongxing Zhang, and X. Liu conducted the sample selection and data management. Haitao Zhang, Y.W., C.Y., and Y. Li performed the SNV genotyping in the replication stages. X. Liu, Z.Z., C.W., H.C., Q.L., S.C., and M.L. performed the functional and mechanism experiments. Y.W., Y. Li, X. Zuo, X. Zhang, and T.Z. analyzed the omics data. Y.W., Y. Li, and X. Liu performed the statistical analyses, interpreted the results, and drafted the manuscript. G.Z. approved the final version of the manuscript.

DECLARATION OF INTERESTS

The authors declare no competing interests.

Received: November 13, 2022
Revised: February 26, 2024
Accepted: April 5, 2024
Published: May 1, 2024

REFERENCES

1. Siegel, R.L., Miller, K.D., and Jemal, A. (2019). Cancer statistics, 2019. C.A. Cancer J. Clin. *69*, 7–34.
2. Cao, P., Yang, A., Wang, R., Xia, X., Zhai, Y., Li, Y., Yang, F., Cui, Y., Xie, W., Liu, Y., et al. (2018). Germline Duplication of SNORA18L5 Increases Risk for HBV-related Hepatocellular Carcinoma by Altering Localization of Ribosomal Proteins and Decreasing Levels of p53. Gastroenterology *155*, 542–556.
3. Jiang, D.K., Sun, J., Cao, G., Liu, Y., Lin, D., Gao, Y.Z., Ren, W.H., Long, X.D., Zhang, H., Ma, X.P., et al. (2013). Genetic variants in STAT4 and HLA-DQ genes confer risk of hepatitis B virus-related hepatocellular carcinoma. Nat. Genet. *45*, 72–75.
4. Kumar, V., Kato, N., Urabe, Y., Takahashi, A., Muroyama, R., Hosono, N., Otsuka, M., Tateishi, R., Omata, M., Nakagawa, H., et al. (2011). Genome-wide association study identifies a susceptibility locus for HCV-induced hepatocellular carcinoma. Nat. Genet. *43*, 455–458.
5. Li, S., Fell, S.M., Surova, O., Smedler, E., Wallis, K., Chen, Z.X., Hellman, U., Johnsen, J.I., Martinsson, T., Kenchappa, R.S., et al. (2016). The 1p36 Tumor Suppressor KIF 1Bbeta Is Required for Calcineurin Activation, Controlling Mitochondrial Fission and Apoptosis. Dev. Cell *36*, 164–178.
6. Li, S., Qian, J., Yang, Y., Zhao, W., Dai, J., Bei, J.X., Foo, J.N., McLaren, P.J., Li, Z., Yang, J., et al. (2012). GWAS identifies novel susceptibility loci on 6p21.32 and 21q21.3 for hepatocellular carcinoma in chronic hepatitis B virus carriers. PLoS Genet. *8*, e1002791.
7. Zhang, H., Zhai, Y., Hu, Z., Wu, C., Qian, J., Jia, W., Ma, F., Huang, W., Yu, L., Yue, W., et al. (2010). Genome-wide association study identifies 1p36.22 as a new susceptibility locus for hepatocellular carcinoma in chronic hepatitis B virus carriers. Nat. Genet. *42*, 755–758.
8. Trépo, E., Caruso, S., Yang, J., Imbeaud, S., Couchy, G., Bayard, Q., Letouzé, E., Ganne-Carrié, N., Moreno, C., Oussalah, A., et al. (2022). Common genetic variation in alcohol-related hepatocellular carcinoma: a case-control genome-wide association study. Lancet Oncol. *23*, 161–171.
9. Jung, S.W., Park, N.H., Shin, J.W., Park, B.R., Kim, C.J., Lee, J.E., Shin, E.S., Kim, J.A., and Chung, Y.H. (2012). Polymorphisms of DNA repair genes in Korean hepatocellular carcinoma patients with chronic hepatitis B: possible implications on survival. J. Hepatol. *57*, 621–627.
10. Xu, W., Liu, S.A., Li, L., Shen, Z.Y., and Wu, Y.L. (2015). Association between XRCC1 Arg280His polymorphism and risk of hepatocellular carcinoma: a systematic review and meta-analysis. Genet. Mol. Res. *14*, 7122–7129.
11. Sazonovs, A., and Barrett, J.C. (2018). Rare-Variant Studies to Complement Genome-Wide Association Studies. Annu. Rev. Genom. Hum. Genet. *19*, 97–112.
12. Kiwerska, K., and Szyfter, K. (2019). DNA repair in cancer initiation, progression, and therapy-a double-edged sword. J. Appl. Genet. *60*, 329–334.
13. Jachimowicz, R.D., Beleggia, F., Isensee, J., Velpula, B.B., Goergens, J., Bustos, M.A., Doll, M.A., Shenoy, A., Checa-Rodriguez, C., Wiederstein,

J.L., et al. (2019). UBQLN4 Represses Homologous Recombination and Is Overexpressed in Aggressive Tumors. Cell *176*, 505–519.e22.

14. Gogola, E., Duarte, A.A., de Ruiter, J.R., Wiegant, W.W., Schmid, J.A., de Bruijn, R., James, D.I., Llobet, S.G., Vis, D.J., Annunziato, S., et al. (2019). Selective Loss of PARG Restores PARylation and Counteracts PARP Inhibitor-Mediated Synthetic Lethality. Cancer Cell *35*, 950–952.
15. Setton, J., Zinda, M., Riaz, N., Durocher, D., Zimmermann, M., Koehler, M., Reis-Filho, J.S., and Powell, S.N. (2021). Synthetic Lethality in Cancer Therapeutics: The Next Generation. Cancer Discov. *11*, 1626–1635.
16. Dias, M.P., Moser, S.C., Ganesan, S., and Jonkers, J. (2021). Understanding and overcoming resistance to PARP inhibitors in cancer therapy. Nat. Rev. Clin. Oncol. *18*, 773–791.
17. Paturel, A., Hall, J., and Chemin, I. (2022). Poly(ADP-Ribose) Polymerase Inhibition as a Promising Approach for Hepatocellular Carcinoma Therapy. Cancers *14*, 3806.
18. Yang, X.D., Kong, F.E., Qi, L., Lin, J.X., Yan, Q., Loong, J.H.C., Xi, S.Y., Zhao, Y., Zhang, Y., Yuan, Y.F., et al. (2021). PARP inhibitor Olaparib overcomes Sorafenib resistance through reshaping the pluripotent transcriptome in hepatocellular carcinoma. Mol. Cancer *20*, 20.
19. Wang, C., Tang, H., Geng, A., Dai, B., Zhang, H., Sun, X., Chen, Y., Qiao, Z., Zhu, H., Yang, J., et al. (2020). Rational combination therapy for hepatocellular carcinoma with PARP1 and DNA-PK inhibitors. Proc. Natl. Acad. Sci. USA *117*, 26356–26365.
20. Vannier, J.B., Sarek, G., and Boulton, S.J. (2014). RTEL1: functions of a disease-associated helicase. Trends Cell Biol. *24*, 416–425.
21. Lespagnol, A., Duflaut, D., Beekman, C., Blanc, L., Fiucci, G., Marine, J.C., Vidal, M., Amson, R., and Telerman, A. (2008). Exosome secretion, including the DNA damage-induced p53-dependent secretory pathway, is severely compromised in TSAP6/Steap3-null mice. Cell Death Differ. *15*, 1723–1733.
22. Wang, Y., Liu, X., Guan, G., Zhao, W., and Zhuang, M. (2019). A Risk Classification System With Five-Gene for Survival Prediction of Glioblastoma Patients. Front. Neurol. *10*, 745.
23. Jiao, A.L., Perales, R., Umbreit, N.T., Haswell, J.R., Piper, M.E., Adams, B.D., Pellman, D., Kennedy, S., and Slack, F.J. (2019). Human nuclear RNAi-defective 2 (NRDE2) is an essential RNA splicing factor. RNA *25*, 352–363.
24. Wang, J., Chen, J., Wu, G., Zhang, H., Du, X., Chen, S., Zhang, L., Wang, K., Fan, J., Gao, S., et al. (2019). NRDE2 negatively regulates exosome functions by inhibiting MTR4 recruitment and exosome interaction. Genes Dev. *33*, 536–549.
25. Chiu, C.G., Nakamura, Y., Chong, K.K., Huang, S.K., Kawas, N.P., Triche, T., Elashoff, D., Kiyohara, E., Irie, R.F., Morton, D.L., and Hoon, D.S.B. (2014). Genome-wide characterization of circulating tumor cells identifies novel prognostic genomic alterations in systemic melanoma metastasis. Clin. Chem. *60*, 873–885.
26. Gao, Q., Zhu, H., Dong, L., Shi, W., Chen, R., Song, Z., Huang, C., Li, J., Dong, X., Zhou, Y., et al. (2019). Integrated Proteogenomic Characterization of HBV-Related Hepatocellular Carcinoma. Cell *179*, 1240.
27. Subramanian, A., Tamayo, P., Mootha, V.K., Mukherjee, S., Ebert, B.L., Gillette, M.A., Paulovich, A., Pomeroy, S.L., Golub, T.R., Lander, E.S., and Mesirov, J.P. (2005). Gene set enrichment analysis: a knowledge-based approach for interpreting genome-wide expression profiles. Proc. Natl. Acad. Sci. USA *102*, 15545–15550.
28. Dietlein, F., Thelen, L., and Reinhardt, H.C. (2014). Cancer-specific defects in DNA repair pathways as targets for personalized therapeutic approaches. Trends Genet. *30*, 326–339.
29. Gunn, A., and Stark, J.M. (2012). I-SceI-based assays to examine distinct repair outcomes of mammalian chromosomal double strand breaks. Methods Mol. Biol. *920*, 379–391.
30. Liu, H., Zhang, H., Wu, X., Ma, D., Wu, J., Wang, L., Jiang, Y., Fei, Y., Zhu, C., Tan, R., et al. (2018). Nuclear cGAS suppresses DNA repair and promotes tumorigenesis. Nature *563*, 131–136.
31. Pilié, P.G., Tang, C., Mills, G.B., and Yap, T.A. (2019). State-of-the-art strategies for targeting the DNA damage response in cancer. Nat. Rev. Clin. Oncol. *16*, 81–104.
32. Alexandrov, L.B., Kim, J., Haradhvala, N.J., Huang, M.N., Tian Ng, A.W., Wu, Y., Boot, A., Covington, K.R., Gordenin, D.A., Bergstrom, E.N., et al. (2020). The repertoire of mutational signatures in human cancer. Nature *578*, 94–101.
33. Rabalski, A.J., Gyenis, L., and Litchfield, D.W. (2016). Molecular Pathways: Emergence of Protein Kinase CK2 (CSNK2) as a Potential Target to Inhibit Survival and DNA Damage Response and Repair Pathways in Cancer Cells. Clin. Cancer Res. *22*, 2840–2847.
34. Olsen, B.B., Wang, S.Y., Svenstrup, T.H., Chen, B.P.C., and Guerra, B. (2012). Protein kinase CK2 localizes to sites of DNA double-strand break regulating the cellular response to DNA damage. BMC Mol. Biol. *13*, 7.
35. Zeytuni, N., and Zarivach, R. (2012). Structural and functional discussion of the tetra-trico-peptide repeat, a protein interaction module. Structure *20*, 397–405.
36. Janicki, S.M., Tsukamoto, T., Salghetti, S.E., Tansey, W.P., Sachidanandam, R., Prasanth, K.V., Ried, T., Shav-Tal, Y., Bertrand, E., Singer, R.H., and Spector, D.L. (2004). From silencing to gene expression: real-time analysis in single cells. Cell *116*, 683–698.
37. Zhou, L., Liang, C., Chen, Q., Zhang, Z., Zhang, B., Yan, H., Qi, F., Zhang, M., Yi, Q., Guan, Y., et al. (2017). The N-Terminal Non-Kinase-Domain-Mediated Binding of Haspin to Pds5B Protects Centromeric Cohesion in Mitosis. Curr. Biol. *27*, 992–1004.
38. Peng, Y., Liao, Q., Tan, W., Peng, C., Hu, Z., Chen, Y., Li, Z., Li, J., Zhen, B., Zhu, W., et al. (2019). The deubiquitylating enzyme USP15 regulates homologous recombination repair and cancer cell response to PARP inhibitors. Nat. Commun. *10*, 1224.
39. Oshima, T., Niwa, Y., Kuwata, K., Srivastava, A., Hyoda, T., Tsuchiya, Y., Kumagai, M., Tsuyuguchi, M., Tamaru, T., Sugiyama, A., et al. (2019). Cell-based screen identifies a new potent and highly selective CK2 inhibitor for modulation of circadian rhythms and cancer cell growth. Sci. Adv. *5*, eaau9060.
40. Ao, Y., Zhang, J., Liu, Z., Qian, M., Li, Y., Wu, Z., Sun, P., Wu, J., Bei, W., Wen, J., et al. (2019). Lamin A buffers CK2 kinase activity to modulate aging in a progeria mouse model. Sci. Adv. *5*, eaav5078.
41. Wu, L., Luo, K., Lou, Z., and Chen, J. (2008). MDC1 regulates intra-S-phase checkpoint by targeting NBS1 to DNA double-strand breaks. Proc. Natl. Acad. Sci. USA *105*, 11200–11205.
42. Melander, F., Bekker-Jensen, S., Falck, J., Bartek, J., Mailand, N., and Lukas, J. (2008). Phosphorylation of SDT repeats in the MDC1 N terminus triggers retention of NBS1 at the DNA damage-modified chromatin. J. Cell Biol. *181*, 213–226.
43. Chapman, J.R., and Jackson, S.P. (2008). Phospho-dependent interactions between NBS1 and MDC1 mediate chromatin retention of the MRN complex at sites of DNA damage. EMBO Rep. *9*, 795–801.
44. Ruff, S.E., Logan, S.K., Garabedian, M.J., and Huang, T.T. (2020). Roles for MDC1 in cancer development and treatment. DNA Repair *95*, 102948.
45. Scully, R., Panday, A., Elango, R., and Willis, N.A. (2019). DNA double-strand break repair-pathway choice in somatic mammalian cells. Nat. Rev. Mol. Cell Biol. *20*, 698–714.
46. Tsherniak, A., Vazquez, F., Montgomery, P.G., Weir, B.A., Kryukov, G., Cowley, G.S., Gill, S., Harrington, W.F., Pantel, S., Krill-Burger, J.M., et al. (2017). Defining a Cancer Dependency Map. Cell *170*, 564–576.e16.
47. Abdolahi, S., Ghazvinian, Z., Muhammadnejad, S., Saleh, M., Asadzadeh Aghdaei, H., and Baghaei, K. (2022). Patient-derived xenograft (PDX) models, applications and challenges in cancer research. J. Transl. Med. *20*, 206.
48. Zhou, J., Sun, H.C., Wang, Z., Cong, W.M., Wang, J.H., Zeng, M.S., Yang, J.M., Bie, P., Liu, L.X., Wen, T.F., et al. (2018). Guidelines for Diagnosis and Treatment of Primary Liver Cancer in China (2017 Edition). Liver Cancer *7*, 235–260.

49. Guang, S., Bochner, A.F., Burkhart, K.B., Burton, N., Pavelec, D.M., and Kennedy, S. (2010). Small regulatory RNAs inhibit RNA polymerase II during the elongation phase of transcription. Nature *465*, 1097–1101.

50. Aronica, L., Kasparek, T., Ruchman, D., Marquez, Y., Cipak, L., Cipakova, I., Anrather, D., Mikolaskova, B., Radtke, M., Sarkar, S., et al. (2016). The spliceosome-associated protein Nrl1 suppresses homologous recombination-dependent R-loop formation in fission yeast. Nucleic Acids Res. *44*, 1703–1717.

51. Richard, P., Ogami, K., Chen, Y., Feng, S., Moresco, J.J., Yates, J.R., 3rd, and Manley, J.L. (2018). NRDE-2, the human homolog of fission yeast Nrl1, prevents DNA damage accumulation in human cells. RNA Biol. *15*, 868–876.

52. Flemr, M., Schwaiger, M., Hess, D., Iesmantavicius, V., Ahel, J., Tuck, A.C., Mohn, F., and Bühler, M. (2023). Mouse nuclear RNAi-defective 2 promotes splicing of weak 5' splice sites. RNA *29*, 1140–1165.

53. Xu, K., Wu, T., Xia, P., Chen, X., and Yuan, Y. (2023). Alternative splicing: a bridge connecting NAFLD and HCC. Trends Mol. Med. *29*, 859–872.

54. Roffey, S.E., and Litchfield, D.W. (2021). CK2 Regulation: Perspectives in 2021. Biomedicines *9*, 1361.

55. Ashworth, A., and Lord, C.J. (2018). Synthetic lethal therapies for cancer: what's next after PARP inhibitors? Nat. Rev. Clin. Oncol. *15*, 564–576.

56. Byrum, A.K., Vindigni, A., and Mosammaparast, N. (2019). Defining and Modulating 'BRCAness. Trends Cell Biol. *29*, 740–751.

57. Huang, K.L., Mashl, R.J., Wu, Y., Ritter, D.I., Wang, J., Oh, C., Paczkowska, M., Reynolds, S., Wyczalkowski, M.A., Oak, N., et al. (2018). Pathogenic Germline Variants in 10,389 Adult Cancers. Cell *173*, 355–370.e14.

58. Okawa, Y., Iwasaki, Y., Johnson, T.A., Ebata, N., Inai, C., Endo, M., Maejima, K., Sasagawa, S., Fujita, M., Matsuda, K., et al. (2023). Hereditary cancer variants and homologous recombination deficiency in biliary tract cancer. J. Hepatol. *78*, 333–342.

59. Li, Y., Zhai, Y., Song, Q., Zhang, H., Cao, P., Ping, J., Liu, X., Guo, B., Liu, G., Song, J., et al. (2018). Genome-Wide Association Study Identifies a New Locus at 7q21.13 Associated with Hepatitis B Virus-Related Hepatocellular Carcinoma. Clin. Cancer Res. *24*, 906–915.

60. Schwantes-An, T.H., Darlay, R., Mathurin, P., Masson, S., Liangpunsakul, S., Mueller, S., Aithal, G.P., Eyer, F., Gleeson, D., Thompson, A., et al. (2021). Genome-wide Association Study and Meta-analysis on Alcohol-Associated Liver Cirrhosis Identifies Genetic Risk Factors. Hepatology *73*, 1920–1931.

61. Tang, H., Jin, X., Li, Y., Jiang, H., Tang, X., Yang, X., Cheng, H., Qiu, Y., Chen, G., Mei, J., et al. (2014). A large-scale screen for coding variants predisposing to psoriasis. Nat. Genet. *46*, 45–50.

62. Kan, Z., Zheng, H., Liu, X., Li, S., Barber, T.D., Gong, Z., Gao, H., Hao, K., Willard, M.D., Xu, J., et al. (2013). Whole-genome sequencing identifies recurrent mutations in hepatocellular carcinoma. Genome Res. *23*, 1422–1433.

63. Jiang, X., Zhang, B., Zhao, J., Xu, Y., Han, H., Su, K., Tao, J., Fan, R., Zhao, X., Li, L., and Li, M.D. (2019). Identification and characterization of SEC24D as a susceptibility gene for hepatitis B virus infection. Sci. Rep. *9*, 13425.

64. Li, H., and Durbin, R. (2010). Fast and accurate long-read alignment with Burrows-Wheeler transform. Bioinformatics *26*, 589–595.

65. McKenna, A., Hanna, M., Banks, E., Sivachenko, A., Cibulskis, K., Kernytsky, A., Garimella, K., Altshuler, D., Gabriel, S., Daly, M., and DePristo, M.A. (2010). The Genome Analysis Toolkit: a MapReduce framework for analyzing next-generation DNA sequencing data. Genome Res. *20*, 1297–1303.

66. Epi, K.c.; Epilepsy Phenome/Genome, P (2017). Ultra-rare genetic variation in common epilepsies: a case-control sequencing study. Lancet Neurol. *16*, 135–143.

67. Wang, K., Li, M., and Hakonarson, H. (2010). ANNOVAR: functional annotation of genetic variants from high-throughput sequencing data. Nucleic Acids Res. *38*, e164.

68. Ioannidis, N.M., Rothstein, J.H., Pejaver, V., Middha, S., McDonnell, S.K., Baheti, S., Musolf, A., Li, Q., Holzinger, E., Karyadi, D., et al. (2016). REVEL: An Ensemble Method for Predicting the Pathogenicity of Rare Missense Variants. Am. J. Hum. Genet. *99*, 877–885.

69. Jagadeesh, K.A., Wenger, A.M., Berger, M.J., Guturu, H., Stenson, P.D., Cooper, D.N., Bernstein, J.A., and Bejerano, G. (2016). M-CAP eliminates a majority of variants of uncertain significance in clinical exomes at high sensitivity. Nat. Genet. *48*, 1581–1586.

70. Kircher, M., Witten, D.M., Jain, P., O'Roak, B.J., Cooper, G.M., and Shendure, J. (2014). A general framework for estimating the relative pathogenicity of human genetic variants. Nat. Genet. *46*, 310–315.

71. Schwarz, J.M., Cooper, D.N., Schuelke, M., and Seelow, D. (2014). MutationTaster2: mutation prediction for the deep-sequencing age. Nat. Methods *11*, 361–362.

72. Galinsky, K.J., Bhatia, G., Loh, P.R., Georgiev, S., Mukherjee, S., Patterson, N.J., and Price, A.L. (2016). Fast Principal-Component Analysis Reveals Convergent Evolution of ADH1B in Europe and East Asia. Am. J. Hum. Genet. *98*, 456–472.

73. Zhan, X., Hu, Y., Li, B., Abecasis, G.R., and Liu, D.J. (2016). RVTESTS: an efficient and comprehensive tool for rare variant association analysis using sequence data. Bioinformatics *32*, 1423–1426.

74. Severe Covid-19 GWAS Group; Ellinghaus, D., Degenhardt, F., Bujanda, L., Buti, M., Albillos, A., Invernizzi, P., Fernández, J., Prati, D., Baselli, G., et al. (2020). Genomewide Association Study of Severe Covid-19 with Respiratory Failure. N. Engl. J. Med. *383*, 1522–1534.

75. Do, R., Stitziel, N.O., Won, H.H., Jørgensen, A.B., Duga, S., Angelica Merlini, P., Kiezun, A., Farrall, M., Goel, A., Zuk, O., et al. (2015). Exome sequencing identifies rare LDLR and APOA5 alleles conferring risk for myocardial infarction. Nature *518*, 102–106.

76. Ghosh, R., Oak, N., and Plon, S.E. (2017). Evaluation of in silico algorithms for use with ACMG/AMP clinical variant interpretation guidelines. Genome Biol. *18*, 225.

77. Tse, K.P., Tsang, N.M., Chen, K.D., Li, H.P., Liang, Y., Hsueh, C., Chang, K.P., Yu, J.S., Hao, S.P., Hsieh, L.L., and Chang, Y.S. (2007). MCP-1 Promoter Polymorphism at 2518 is associated with metastasis of nasopharyngeal carcinoma after treatment. Clin. Cancer Res. *13*, 6320–6326.

78. Gao, Q., Zhu, H., Dong, L., Shi, W., Chen, R., Song, Z., Huang, C., Li, J., Dong, X., Zhou, Y., et al. (2019). Integrated Proteogenomic Characterization of HBV-Related Hepatocellular Carcinoma. Cell *179*, 1240–1577.e522.

79. Langmead, B., and Salzberg, S.L. (2012). Fast gapped-read alignment with Bowtie 2. Nat. Methods *9*, 357–359.

80. Li, B., and Dewey, C.N. (2011). RSEM: accurate transcript quantification from RNA-Seq data with or without a reference genome. BMC Bioinf. *12*, 323.

81. Love, M.I., Huber, W., and Anders, S. (2014). Moderated estimation of fold change and dispersion for RNA-seq data with DESeq2. Genome Biol. *15*, 550.

82. Zhou, Y., Zhou, B., Pache, L., Chang, M., Khodabakhshi, A.H., Tanaseichuk, O., Benner, C., and Chanda, S.K. (2019). Metascape provides a biologist-oriented resource for the analysis of systems-level datasets. Nat. Commun. *10*, 1523.

83. Mao, Z., Hine, C., Tian, X., Van Meter, M., Au, M., Vaidya, A., Seluanov, A., and Gorbunova, V. (2011). SIRT6 promotes DNA repair under stress by activating PARP1. Science *332*, 1443–1446.

84. Jin, B.F., He, K., Wang, H.X., Wang, J., Zhou, T., Lan, Y., Hu, M.R., Wei, K.H., Yang, S.C., Shen, B.F., and Zhang, X.M. (2003). Proteomic analysis of ubiquitin-proteasome effects: insight into the function of eukaryotic initiation factor 5A. Oncogene *22*, 4819–4830.

85. Tyanova, S., Temu, T., and Cox, J. (2016). The MaxQuant computational platform for mass spectrometry-based shotgun proteomics. Nat. Protoc. *11*, 2301–2319.

86. Yang, J., Yan, R., Roy, A., Xu, D., Poisson, J., and Zhang, Y. (2015). The I-TASSER Suite: protein structure and function prediction. Nat. Methods *12*, 7–8.

87. Rodrigues, C.H., Pires, D.E., and Ascher, D.B. (2018). DynaMut: predicting the impact of mutations on protein conformation, flexibility and stability. Nucleic Acids Res. *46*, W350–W355.

88. Han, J., Yu, M., Bai, Y., Yu, J., Jin, F., Li, C., Zeng, R., Peng, J., Li, A., Song, X., et al. (2020). Elevated CXorf67 Expression in PFA Ependymomas Suppresses DNA Repair and Sensitizes to PARP Inhibitors. Cancer Cell *38*, 844–856.e7.

89. Cox, J., Neuhauser, N., Michalski, A., Scheltema, R.A., Olsen, J.V., and Mann, M. (2011). Andromeda: a peptide search engine integrated into the MaxQuant environment. J. Proteome Res. *10*, 1794–1805.

90. Lachmann, A., and Ma'ayan, A. (2009). KEA: kinase enrichment analysis. Bioinformatics *25*, 684–686.

91. Cheng, A., Grant, C.E., Noble, W.S., and Bailey, T.L. (2019). MoMo: discovery of statistically significant post-translational modification motifs. Bioinformatics *35*, 2774–2782.

92. Sun, J., Belke, D., Gui, Y., Chen, Y.-X., Zhou, S., and Zheng, X.-L. (2023). Polo-like kinase 4 inhibitor CFI-400945 inhibits carotid arterial neointima formation but increases atherosclerosis. Cell Death Dis. *9*, 49.

93. Rosenthal, R., McGranahan, N., Herrero, J., Taylor, B.S., and Swanton, C. (2016). DeconstructSigs: delineating mutational processes in single tumors distinguishes DNA repair deficiencies and patterns of carcinoma evolution. Genome Biol. *17*, 31.

94. Menashe, I., Rosenberg, P.S., and Chen, B.E. (2008). PGA: power calculator for case-control genetic association analyses. BMC Genet. *9*, 36.

STAR★METHODS

KEY RESOURCES TABLE

REAGENT or RESOURCE	SOURCE	IDENTIFIER
Antibodies		
Anti-ATM	Cell Signaling Technology	Cat#2873T; RRID: AB_2062659
Anti-ATR	Cell Signaling Technology	Cat#2790S; RRID: AB_2227860
Anti-CHK1	Cell Signaling Technology	Cat#2360S; RRID: AB_2080320
Anti-CHK2	Cell Signaling Technology	Cat#3440S; RRID: AB_2229490
Anti-CK2A1	Proteintech	Cat#10992-1-AP; RRID: AB_2245531
Anti-CK2A2	Proteintech	Cat#10606-1-AP; RRID: AB_2292447
Anti-CK2B	Proteintech	Cat# 20234-1-AP; RRID: AB_10733246
Anti-CK2 phosphorylation	Cell Signaling Technology	Cat#8738; RRID: AB_2797653
Anti-Flag	Sigma-Aldrich	Cat#F3165; RRID: AB_259529
Anti-GST	Abcam	Cat#ab92; RRID: AB_307067
Anti-HA	MBL	Cat#M180-3; RRID: AB_10951811
Anti-Histone-H3	Proteintech	Cat#17168-1-AP; RRID: AB_2716755
Anti-MDC1	Nouvs Biologicals	Cat#NB100-395; RRID: AB_10001489
Anti-MRE11	Proteintech	Cat#10744-1-AP; RRID: AB_2145118
Anti-MTR4	Proteintech	Cat#12719-2-AP; RRID: AB_2187479
Anti-MYH9	Proteintech	Cat#11128-1-AP; RRID: AB_2147294
Anti-Myc	Proteintech	Cat#60003-2-Ig; RRID: AB_2734122
Anti-NBS1	Proteintech	Cat#55025-1-AP; RRID: AB_2734122
Anti-NPM1	Proteintech	Cat#10306-1-AP; RRID: AB_2155163
Anti-NRDE2	Proteintech	Cat#24968-1-AP; RRID: AB_2879825
Anti-pan p-S/T	ABclonal	Cat#AP1067; RRID: AB_2863939
Anti-*p*-ATR	Cell Signaling Technology	Cat#2853T; RRID: AB_2290281
Anti-*p*-ATM	Cell Signaling Technology	Cat#5883T; RRID: AB_10835213
Anti-*p*-CHK1	Cell Signaling Technology	Cat#2348T; RRID: AB_331212
Anti-*p*-CHK2	Cell Signaling Technology	Cat#2197S; RRID: AB_2080501
Anti-*p*-MDC1 (Thr378)	This paper	RRID: AB_3096307
Anti-RAD50	Proteintech	Cat#29390-1-AP; RRID: AB_2918289
Anti-RAD51	Abcam	Cat#ab88572; RRID: AB_2042762
Anti-RANBP17	Affinity	Cat#DF4379; RRID: AB_2836667
Anti-RPA2	Proteintech	Cat#10412-1-AP; RRID: AB_2269665
Anti-RTEL1	Proteintech	Cat#25337-1-AP; RRID: AB_2880034
Anti-STEAP3	Proteintech	Cat#17186-1-AP; RRID: AB_2197841
Anti-53BP1	Novus Biologicals	Cat#NB100-304; RRID: AB_10003037
Anti-β-actin	Proteintech	Cat#60008-1-Ig; RRID: AB_2289225
Anti-γ-H2AX	Millipore	Cat#05-636; RRID: AB_309864
Goat anti-rabbit IgG	Cwbiotech	Cat#CW0103; RRID: AB_2814709
Goat anti-mouse IgG	Cwbiotech	Cat#CW0102; RRID: AB_2814710
Chemicals, peptides, and recombinant proteins		
Camptothecin	Selleck	Cat#S1288
Oxaliplatin	Selleck	Cat#S1224
Olaparib	Selleck	Cat#S1060
Cell staining buffer	Biolegend	Cat#420201
SYBR Green Universal PCR Master Mix	KAPA	Cat#KR0389-v8.12

(*Continued on next page*)

Continued

REAGENT or RESOURCE	SOURCE	IDENTIFIER
Protease inhibitor cocktail	Roche	Cat#4693116001
Polybrene	Sigma	Cat#H9268
Gateway™ LR Clonase™ II Enzyme mix	Thermo Fisher	Cat#11791100
Gateway™ BP Clonase™ II Enzyme mix	Thermo Fisher	Cat#11789100
Cycloheximide	Sigma	Cat#C7698
MG132	Sigma	Cat#M8699
Lipofectamine 3000	Invitrogen	Cat#L3000-015
Puromycin	Merk	Cat#540411
L-Glutathione reduced	Sigma	Cat#G4251
Streptavidin-conjugated beads	GE Healthcare	Cat#28-9857-99
Glutathione Sepharose	Merk	Cat#G4510
Critical commercial assays		
Cell Fractionation Kit	Cell Signaling	Cat#9038
Cell Counting Kit-8 (CCK-8)	Dojindo	Cat#ck04
Deposited data		
Whole-exome sequencing data	This paper	National Genomics Data Center (NGDC: GVM000716, https://bigd.big.ac.cn/gvm/getProjectDetail?Project=GVM000716)
Mass spectrometry-based protein interactome and phosphoproteomics data	This paper	ProteomeXchange (PXD051117, https://proteomecentral.proteomexchange.org/cgi/GetDataset?ID=PXD051117) or iProX (IPX0005489000, https://www.iprox.cn/page/project.html?id=IPX0005489000)
RNA sequencing raw data	This paper	Genome Sequence Archive (GSA-Human: HRA005351, https://ngdc.cncb.ac.cn/gsa-human/browse/HRA005351)
Experimental models: Cell lines		
HepG2	China Center for Type Culture Collection	N/A
Huh-7	China Center for Type Culture Collection	N/A
U2OS	China Center for Type Culture Collection	N/A
U2OS-LacO	Zhou et al.[37]	N/A
U2OS DR-GFP	Peng et al.[38]	N/A
U2OS EJ5-GFP	Peng et al.[38]	N/A
HEK293T	China Center for Type Culture Collection	N/A
Experimental models: Organisms/strains		
Mouse: BALB/c Nude Mice	Charles River	Strain code: 401
NRDE2-WT PDX #1	The fifth Medical Center of Chinese PLA General Hospital	N/A
NRDE2-N377I PDX #1	IDMO Co., Ltd	N/A
NRDE2-WT PDX #2	The fifth Medical Center of Chinese PLA General Hospital	N/A
NRDE2-N377I PDX #2	IDMO Co., Ltd	N/A
Oligonucleotides		
PCR primers	This paper	Table S5
siRNAs and shRNAs	This paper	Table S5
Recombinant DNA		
GFP/Myc-LacR	Zhou et al.[37]	NA
pcDNA3.1	Invitrogen	Cat#V79020
pLV *Neo*	Inovogen	N/A
pCMV-Myc	Clontech	Cat#631604

(*Continued on next page*)

Continued

REAGENT or RESOURCE	SOURCE	IDENTIFIER
Software and algorithms		
ANNOVAR (20150322)	Wang et al.[67]	https://annovar.openbioinformatics.org/en/latest/
Bowtie2	Langmead et al.[79]	https://github.com/BenLangmead/bowtie2
BWA (v0.7)	Li et al.[64]	https://github.com/lh3/bwa
DeconstructSigs	Rosenthal et al.[93]	https://github.com/raerose01/deconstructSigs
DepMap	Tsherniak et al.[46]	https://depmap.org/portal/
DESeq2	Love et al.[81]	https://github.com/thelovelab/DESeq2
DynaMut	Rodrigues et al.[87]	http://biosig.unimelb.edu.au/dynamut/
EIGENSOFT (v3)	Galinsky et al.[72]	https://www.hsph.harvard.edu/alkes-price/software/
FlowJo (v9.8.1)	TreeStar	https://www.flowjo.com/solutions/flowjo
GATK (v3.6)	McKenna et al.[65]	https://gatk.broadinstitute.org/hc/en-us
GraphPad Prism 8	GraphPad Software	https://www.graphpad.com
GSEA (v4.1)	Subramanian et al.[27]	http://software.broadinstitute.org/gsea
IGV	Broad Institute	http://software.broadinstitute.org/software/igv/
ImageJ (v1.8.0)	National Institute of Health	https://imagej.nih.gov/ij
I-TASSER	Yang et al.[86]	https://seq2fun.dcmb.med.umich.edu//I-TASSER/
KEA	Lachmann et al.[90]	https://www.maayanlab.net/KEA2/
MassARRAY Assay Design 3.0	Sequenom	https://www.agenabio.com/products/massarray-system/
MaxQuant (v1.5.3.8)	Tyanova et al.[85]	https://www.maxquant.org/
Metascape	Zhou et al.[82]	https://metascape.org/gp/index.html
MoMo	Cheng et al.[91]	https://meme-suite.org/meme/tools/momo
PGA	Menashe et al.[94]	https://dceg.cancer.gov/tools/design/pga
Picard (v2.14)	Broad Institute	https://broadinstitute.github.io/picard/
PyMOL	DeLano Scientific	https://pymol.org/2/
RSEM	Li et al.[80]	https://github.com/deweylab/RSEM
RVTESTS (v2.0.5)	Zhan et al.[73]	http://zhanxw.github.io/rvtests/
R (v 3.6.0)	CRAN	https://cran.r-project.org/

RESOURCE AVAILABILITY

Lead contact

Further information and request for resources and reagents should be directed to and will be fulfilled by the lead contact, Dr. Gang-qiao Zhou (zhougq114@126.com).

Materials availability

The plasmids generated in this study have not been deposited to any repositories yet; however, these materials would be available upon request.

Data and code availability

The RNA sequencing dataset of enforced expression of *NRDE2* in Huh-7 cells in this study has been deposited in the Genome Sequence Archive (GSA-Human: HRA005351) that are publicly accessible at https://ngdc.cncb.ac.cn/gsa-human. The publicly available datasets used in this study are from the GEO (GSE76427, GSE63018, GSE364 and GSE56140) and The Cancer Genome Atlas (TCGA). The human genotype data of whole-exome sequencing are available at the National Genomics Data Center (NGDC: GVM000716). The mass spectrometry-based protein interactome and phosphoproteomics data are available at the ProteomeXchange (PXD051117) and iProX (IPX0005489000) databases. This study does not generate any new code.

EXPERIMENTAL MODEL AND SUBJECT DETAILS

Human subjects

In this study, we performed a two-stage rare-variant association study (RVAS) for risk of hepatocellular carcinoma (HCC) in Chinese populations, totally consisting of 2,750 HCC patients (cases) and 4,153 cancer-free subjects (controls) (before quality controls). The discovery stage consisted of 361 cases and 1,757 controls from southern China (Table S1). All the cases in the discovery stage were chronic hepatitis B virus (HBV) carriers with HCC, who are defined as subjects positive for both hepatitis B surface antigen and antibody immunoglobulin G to hepatitis B core antigen for at least 6 months, while the HBV status of the controls was unknown. In this way, genetic association studies based on the HBV-related HCCs and healthy controls are very likely to identify the genes and their SNPs involved in viral infection, but not cancer development. To avoid this bias, in the replication stages, we only used the HBV-related HCCs as the cases, and the chronic HBV carriers without HCC as the controls. The replication stage I included two case-control populations (Shanghai population and Guangxi population, respectively; Table S1). The Shanghai population consisted of 672 cases and 768 controls (designated as replication stage Ia), and the Guangxi population consisted of 794 cases and 742 controls (designated as replication stage Ib). The replication stage II included one case-control population (Shanxi population), consisting of 923 cases and 886 controls (Table S1). The diagnosis of HCC was described in detail previously.[59] Briefly, all the HCC patients were incident HCC cases, and were recruited at the time of their initial diagnosis. The HCC cases were previously untreated (chemotherapy or radiotherapy), and proved not to have other types of cancer. The diagnosis of HCC was made by either positive histologic findings or an elevated serum α-fetoprotein level ($\geq$400 ng/mL) combined with at least one positive image on angiography, sonography, and/or high-resolution contrast computed tomography. All the subjects in this study were chronic HBV carriers except where noted otherwise, who are defined as subjects positive for both hepatitis B surface antigen and antibody immunoglobulin G to hepatitis B core antigen for at least 6 months. The diagnosis of cirrhosis for the cases in the discovery stage was made according to the previous study[60]: (1) clinically evident portal hypertension or decompensated cirrhosis (e.g., ascites, esophageal varices), (2) fibroscan stiffness >22 kPa if aspartate aminotransferase (AST) < 100 IU/L or fibroscan stiffness >32 kPa if AST 100–200 IU/L, or 3) liver histology (Metavir score of F4) on a previously-performed liver biopsy. All subjects included in this study were negative for antibodies to hepatitis C virus, hepatitis D virus, or human immunodeficiency virus; and had no other types of liver disease, such as autoimmune hepatitis, toxic hepatitis, and primary biliary cirrhosis or Budd-Chiari syndrome. This study was performed with the approval of the Medical Ethical Committee of Beijing Institute of Radiation Medicine (Beijing, China) and the corresponding hospitals from that the case-control populations were recruited. Written informed consent was obtained from each participant and/or their guardians.

Southern China population (discovery stage)

This population contained a total of 361 cases and 1,757 controls from southern China. Among the 361 cases, 280 ones were recruited by our groups between November 2009 and July 2012 from the General Hospital of Eastern Theater Command (Nanjing city, Jiangsu province, China) and the First Affiliated Hospital of Zhejiang University (Hangzhou city, Zhejiang province, China). These samples were subjected to whole-exome sequencing (WES) in the present study. Among the 1,757 controls, 1,457 ones without known HBV infection status were recruited by our groups between 1980 and 2006 at the First Affiliated Hospital of Anhui Medical University (Hefei city, Anhui province, China), and have been subjected to WES previously.[61] To increase the statistical power, we further combined two publicly available datasets from European Nucleotide Archive (ENA) database (PRJEB2869 and PRJNA553618), which consisted of 81 cases[62] and 300 controls,[63] all of whom were from southern China. The 81 cases were recruited between 1980 and 2006 at Queen Mary Hospital (Hongkong, China), and have been subjected to whole-genome sequencing (WGS) previously.[62] The 300 controls were recruited between 2010 and 2012 at the First Affiliated Hospital of Zhejiang University School of Medicine and other neighbor medical hospitals or centers (Hangzhou city, Zhejiang province, China), and have been subjected to WES previously.[63] Thus, a total of 361 cases and 1,757 controls were included in the discovery stage. After quality controls as described later, a total of 348 cases and 1,749 controls survived for further analyses (Table S1). Among the 348 cases, 202 ones were HCC patients with cirrhosis, 120 ones were HCC patients without cirrhosis, and other 26 ones had no information of cirrhosis. The male/female ratio of the cases and controls were 6.3 (300/48) and 1.7 (1,102/647), respectively ($p = 7.81 \times 10^{-17}$). The mean age (s.d.) of the cases and controls were 46.0 (11.8) and 33.7 (12.47) years old, respectively ($p = 1.86 \times 10^{-60}$; Table S1).

Shanghai population (replication stage Ia)

This population consisted of 672 cases and 768 controls, who were recruited between June 2011 and July 2013 from Zhongshan Hospital, Shanghai Medical College of Fudan University (Shanghai, China). The response rates for the cases and controls were 92% and 90%, respectively. The male/female ratio of the cases and controls were 3.5 (523/149) and 3.2 (585/183) years old, respectively ($p > 0.05$). The mean age (s.d.) of the cases and controls were 52.41 (9.70) and 49.58 (10.12) years old, respectively ($p = 7.77 \times 10^{-8}$; Table S1).

Guangxi population (replication stage Ib)

This population consisted of 794 cases and 742 controls. These subjects were consecutively recruited between January 2004 to September 2016 at the Guangxi Cancer Hospital (Nanning city, Guangxi province, China). The response rates for the cases and controls in Guangxi population were 92% and 94%, respectively. The male/female ratio of the cases and controls were 8.0 (706/88) and 1.9 (489/253), respectively ($p = 6.19 \times 10^{-28}$; Table S1). The mean age (s.d.) of the cases and controls were 48.69 (11.73) and 42.64 (12.64) years old, respectively ($p = 4.44 \times 10^{-16}$; Table S1).

Shanxi population (replication stage II)

This population consisted of 923 cases and 886 controls. The cases were recruited between June 2011 and July 2013 at Xijing Hospital and Tangdu Hospital, Air Force Medical University (Xi'an city, Shanxi province, China) in northwestern China. The controls were recruited at School of Medicine, Xizang Minzu University (Xi'an city, Shanxi province, China) between December 2011 and July 2012. The response rates for the cases and controls were 92% and 90%, respectively. The male/female ratio and the mean age (s.d.) of cases were 3.3 (709/214) and 51.0 (10.5) years old, respectively. The male/female ratio and the mean age (s.d.) of controls were 0.7 (382/504) and 40.9 (14.1) years old, respectively (Table S1). In this population, cases showed significantly older age ($p = 0.006$), and there were more males in cases than in controls ($p = 1.86 \times 10^{-49}$; Table S1).

In the single-variant-based association analyses, all the cases and controls in replication stages Ia, Ib and II were used in the replication studies, and were genotyped by Sequenom or Kompetitive Allele Specific PCR (KASP) assays. In the gene-based association analyses, the cases and controls from the replication stages Ia and Ib (i.e., Shanghai population and Guangxi population) were subjected to target region high-throughput DNA sequencing in the replication study (Table S1).

Animal studies

Nude mice (BALB/c, male, 4–6 weeks old, Beijing Vital River Laboratory Animal Technology Co., Ltd, Beijing, China) or NPI mice for patient-derived xenografts (PDX) models (NOD-Prkdc^{em1Idmo}Il2rg^{em2Idmo}, male, 4–6 weeks old, IDMO Co., Ltd, Beijing, China) were used for xenograft experiments. All animals received human care and all animal experiments were performed in accordance with the guidelines of the Institutional Animal Care and Use Committee of National Center for Protein Sciences (NCPS; Beijing, China).

Cell lines

The immortalized human liver cancer cell lines HepG2, Huh-7, Hep3B, JHH2, LM3, MHCC97-H, PLC and SNU475, as well as HEK293T and U2OS cell lines, were obtained from the China Center for Type Culture Collection (CCTCC; Wuhan City, China). All the cell lines were maintained in Dulbecco's modified Eagle's medium (DMEM; Gibco, Grand Island, NY, USA) supplemented with 2 mM L-glutamine, 10% fetal bovine serum (FBS; Gibco, Grand Island, NY, USA) and 1% antibiotics (100 U/mL penicillin and 0.1 mg/mL streptomycin). The cells were incubated at 37°C in a humidified incubator containing 5% CO_2.

METHOD DETAILS

High-throughput DNA sequencing, variants calling and quality controls

The discovery stage included a total of 361 cases and 1,757 controls. Among them, 280 cases were recruited by our groups in the present study, and were subjected to WES. Genomic DNA was extracted from the peripheral whole blood of these individuals using standard laboratory procedures. Two micrograms (μg) of DNAs were sheared to ~100–400 base-pair (bp) fragments and processed using Illumina paired-end DNA library preparation. All libraries were sequenced on the Illumina HiSeq 2000 or Illumina HiSeq X Ten sequencer with 100 base paired-end reads. The 1,457 controls have been subjected to WES by our groups previously.[61] To increase the statistical power, we further downloaded the WGS data of 81 cases[62] and WES data of 300 cancer-free controls[63] from the ENA database (PRJEB2869 and PRJNA553618, respectively). The mean coverage was >30× across the targeted protein-coding regions in these datasets.

Next, we pooled the WES and WGS data, and performed sequence alignments and quality controls together. Low quality sequencing reads were removed using the Illumina Genome Analyzer pipeline. The remaining raw reads were mapped to the reference genome (hg19) using Burrows-Wheeler Aligner (BWA v0.7) mem algorithm,[64] and the duplicate fragments were marked using Picard (v2.14). We observed no significant difference of sequencing depth across coding regions and splice-site regions between WES and WGS ($p = 0.66$). We also observed no significant difference in sequencing depth between the cases and controls ($p = 0.08$).

To reduce the potential biases due to processing of case and control data separately, we performed the joint variants calling of all the samples simultaneously. The germline variants calling was performed using the best practice pipeline of the Genome Analysis Toolkit (GATK v3.6).[65] All samples were individually called using Haplotype Caller, and jointly called using GenotypeVCFs with default settings, respectively. In the present study, we focus on the variants in the coding regions and splicing site regions (i.e., intronic positions within 6 bp of exon/intron boundary) in the subsequent analyses.

We then applied the strict variant-level quality controls to detect the high-confidence single nucleotide variants (SNVs) and insertions or deletions (indels)[66]: (i) SNVs/indels were retained if they met the criteria in GATK: depth (DP) < 10, Quality By Depth (QD) < 2.0, Fisher Strand (FS) > 60.0, Mapping Quality (MQ) < 40.0, Mapping Quality Rank Sum (MQRankSum) < −10.5 and Read Position Rank Sum (ReadPosRankSum) < −3.0; (ii) SNVs/indels were retained if they had a call rate of ≥90% and had a Hardy-Weinberg test p value of $>1.0 \times 10^{-4}$; (iii) SNVs/indels were eliminated if they were located in a "universal mask" region defined by Mallick (regions that had either low mappability, low complexity, or were enriched in aberrant variant calls in the 1000 Genomes Project); (iv) SNVs/indels were eliminated if they were located at major histocompatibility complex (MHC) homologous sequence; and (v) SNVs/indels were eliminated if they presented in the false positive sites set defined by publicly available population genetic databases, including the Exome Aggregation Consortium (ExAC) and the Genome Aggregation Database (gnomAD). All variants were annotated by ANNOVAR (20150322),[67] and the potential functional effects of variants were predicted by Rare Exome Variant Ensemble Learner (REVEL),[68] Mendelian Clinically Applicable Pathogenicity (M-CAP),[69] Combined Annotation Dependent Depletion (CADD),[70] and

MutationTaster.[71] Thus, a total of 172,206 autosome non-synonymous SNVs and 14,725 indels were retained. In the present study, we only focused on the rare SNVs/indels, which were defined as SNVs/indels with a minor allele frequency (MAF) of <1% in East Asians population from ExAC or gnomAD databases. Thus, a total of 142,547 rare non-synonymous SNVs/indels were finally retained.

Next, we performed sample-level quality controls. Samples were removed if they: (i) had an average sequencing depth of <10× (including 3 cases); (ii) had less than 90% of the coding regions covered by ≥ 8× (0 samples); (iii) showed sex discrepancies (0 samples); (iv) showed unexpected duplicates or relatives (5 cases); (v) had an overall genotyping rate of <90% (4 cases and 5 controls, respectively); or (vi) were identified as outliers (1 case and 3 controls, respectively). After these quality controls, a total of 348 cases and 1,749 controls survived finally for subsequent analyses.

To evaluate the potential population stratification of cases and controls in the discovery stage, we performed principal component analysis (PCA) by EIGENSOFT (v3).[72] We used the common single nucleotide polymorphisms (SNPs) in exome regions (n = 20,032) for PCA based on the following criteria: call rate >97%, p value of Hardy-Weinberg Equilibrium $>10^{-4}$, and MAF >5%. Ten principal components were estimated for all cases and controls in the discovery stage and all samples from 1000 Genomes Project Phase III (n = 2,504). Using PCA, we found that all cases and controls were of Chinese ancestry.

RVAS in the discovery stage

RVAS on HCC risk were performed by RVTESTS (v2.0.5)[73] using two different strategies, i.e., single-variant-based and gene-based association analyses. These analyses focused on the 142,547 rare nonsynonymous variants. In the single-variant-based tests, all rare nonsynonymous variants (n = 142,547) were analyzed by Fishers' test, leading to the exome-wide significance threshold $p = 5.0 \times 10^{-7}$ (0.05/142,547). Only one SNVs showed exome-wide significant association. Thus, we also defined a suggestive significance threshold $p = 1.0 \times 10^{-5}$, which was widely used in previous studies.[74] Finally, a total of fourteen SNVs showed suggestive associations.

In the gene-based analyses, considering that the gene-based analyses should only contain the deleterious variants and ignore benign variants,[75] we first classified all the rare non-synonymous variants into two sets according to the predicted deleterious effects, and then performed "deleterious" analyses and "disruptive" analyses, respectively.[75] The two sets were: (1) "deleterious" variants, which include the nonsense, splice-site variants, frameshift indels and a subset of missense variants which were predicted as "deleterious" or "damaging" by REVEL,[68] M-CAP,[69] or STRICT[76] methods; and (2) "disruptive" variants, which include the nonsense, splice-site variants and frameshift indels. Then, the gene-based analyses were performed for these remained variants using the combined multivariate and collapsing (CMC) burden test implemented in RVTESTS (v2.0.5). The association results were merged as one association genes list and only the items with less p values for duplicate genes were retained. The significance threshold was defined as $p = 1 \times 10^{-6}$ (0.05/20,203/2). Finally, seven genes showed significant associations in "deleterious" analyses and one gene in "disruptive" analyses, respectively.

Single-variant-based replication studies

In single-variant-based analyses, a total of 14 candidate variants showed suggestive associations with HCC risk in the discovery stage (all $p < 1.0 \times 10^{-5}$), and were selected for follow-up replication analyses. In replication stage I (including the Shanghai population and Guangxi population), these 14 SNVs were genotyped using the Sequenom MassARRAY System according to the manufacturer's instructions (Sequenom, CA, USA). Briefly, the locus-specific polymerase chain reaction (PCR) and detection primers were designed using the MassARRAY Assay Design 3.0 software (Sequenom; Table S5). Approximately 15 ng of genomic DNAs for each sample were amplified by multiplex PCR, and the PCR products were then used for locus-specific single-base extension reactions. The resulting products were desalted and transferred to a 384-element SpectroCHIP array. Allele detection was performed using Matrix-assisted laser desorption/ionization-time of flight (MALDI-TOF) mass spectrometry (MS). The mass spectrograms were analyzed by the MassARRAY TYPER software (Sequenom). The cluster patterns of the genotyping data from Sequenom analyses were visually checked to confirm their good quality. For further quality control, 5% of the individuals in this stage were randomly selected for repeated genotyping, and the results were 100% concordant.

Four SNVs showed significant association ($p < 0.05$) in the replication I, and were further genotyped in the replication stage II (including the Shanxi population). The case-control population in replication stage II was genotyped using the Kompetitive Allele Specific PCR (KASP) system according to the manufacturer's protocol (LGC Genomics, England; http://www.lgcgenomics.com, former KBioscience) by Tsingke Biotechnology Co., Ltd. (Beijing, China). The KASP allele-specific forward primers and common reverse primer were designed by Kraken assay design and workflow management software (LGC Genomics). Results were analyzed by KlusterKaller software according to standard protocols and quality controls (LGC Genomics). For further quality controls, 5% of the individuals in this stage were randomly selected for repeated genotyping, and the results were 100% concordant.

Gene-based replication studies

In gene-based association analyses, a total of eight candidate genes that reached the exome-wide significance ($p < 1.0 \times 10^{-6}$) in discovery stage were subject to replication Ia stage using high-throughput target region re-sequencing. Then, two genes (*RTEL1* and *STEAP3*) that reached significance in replication Ia stage (both $p < 0.05$ and with the same direction as in the discovery stage) were retained for re-sequencing in replication Ib stage. Besides, *NRDE2*, which exhibits the top association signal in single-variant-based analyses (rs199890497), also reached suggestive significance in gene-based association analyses in discovery stage

($p < 1.0 \times 10^{-5}$). Therefore, this gene was also subjected to replication Ia and Ib stages using high-throughput target region re-sequencing. PCR primers were designed, tested and optimized to target the exons and their flanking 10 bp non-coding sequences for each gene. The PCR products were sequenced using the Illumina NovaSeq 6000 sequencer. The mean coverage was >150× across the target regions. Paired-end reads were mapped to the reference genome (hg19) using the BWA (v0.7). Variants were detected by the GATK (v3.6) and annotated using ANNOVAR (v20150322). After variants calling, the variants were reviewed by Integrative Genomics Viewer (IGV) software to ensure the quality and accuracy of the variant calls. Quality controls and association analyses were performed using the same workflow as that in the discovery stage.

Quantitative real-time PCR (qRT-PCR) assays

RNA samples were isolated using the RNeasy mini kit (Qiagen, Hilden, Germany) and were reverse transcribed into cDNAs with the high-capacity cDNA reverse transcription kit (Life Technologies, CA, USA). Quantitative real-time PCR (qRT-PCR) assays were performed with iQ SYBR Green Supermix (#170–8862; Bio-Rad, CA, USA) on an iQ5 real-time PCR detection system (Bio-Rad, CA, USA). Each gene was assessed at least in triplicate using the ΔΔCt method using *β-actin* (*ACTB*) as an internal control. The sequences of the primers were designed using Primer3 (v.0.4.0, http://bioinfo.ut.ee/primer3-0.4.0) and listed in Table S5.

Knockdown or enforced expression of genes

To transiently knock down of human *NRDE2*, *RTEL1*, *RANBP17*, *STEAP3*, *CK2A1*, *CK2A2*, *CK2B*, *MDC1* and *NPM1* genes, the small interfering RNA (siRNA) targeting these genes, and a non-targeting control siRNA were synthesized by RiboBio Co., Ltd. (Guangzhou city, China) (Table S5). The cells were transfected twice with 50 nM siRNAs using riboFECT according to the manufacturer's instructions (RiboBio, Guangzhou city, China).

To stably knock down *NRDE2*, lentiviral small hairpin RNA (shRNA) constructs (pLV-puro-Luciferase) coding a scramble sequence and 2 independent sequences targeting human *NRDE2* genes were obtained from Hanbio Co., Ltd. (Shanghai, China). The vectors with shRNAs along with viral packaging plasmids (PMD and SPA) were transfected into human embryonic kidney HEK293T cells using Lipofectamine 2000 following the manufacturer's instructions (Invitrogen, USA). Virus supernatant was harvested after 48 h, filtered through a 0.45 μM filter, and incubated on target cells for 6 h at a 1:10 dilution with 8 μg/mL polybrene. Infected cells were selected using 200 μg/mL puromycin for 2 weeks before evaluation for efficiency of genes knockdown. All the media contained 10% fetal bovine serum (FBS), 100 units/mL penicillin, and 100 mg/mL streptomycin (15140-122; Gibco, USA). Cells were incubated in humidified incubators equilibrated with 5% CO_2 at 37°C.

The cDNAs encoding human *NRDE2*, *CK2A1*, *CK2A2*, *CK2B* and *MDC1* genes were purchased from Youbio Tech Co., Ltd. (Changsha city, China). The mutations in *NRDE2* and *MDC1* were generated using the QuickChange site-directed mutagenesis kit (Stratagene, CA, USA). To establish the cells with transiently enforced expression of these genes, the eukaryotic expression vector pcDNA3.1 (+) (Invitrogen, USA) was used for enforced expression of these genes. To establish the cells with stably enforced NRDE2-WT or NRDE2-N377I expression, lentivirus packing expression vectors (pLent-CMV-Flag) of NRDE2-WT and NRDE2-N377I were constructed by Vigenebio Co., Ltd. (Jinan city, Shandong province, China). The vectors with NRDE2-WT or NRDE2-N377I along with viral packaging plasmids (PMD and SPA) were transfected into human embryonic kidney HEK293T cells using Lipofectamine 2000 following the manufacturer's instructions (Invitrogen, USA). Virus supernatant was harvested after 48 h, filtered through a 0.45-μM filter, and incubated on target cells for 6 h at a 1:10 dilution with 8 μg/mL polybrene. Infected cells were selected using 200 μg/mL puromycin for 2 weeks before evaluation for efficiency of genes knockdown. All the media contained 10% fetal bovine serum (FBS), 100 units/mL penicillin, and 100 mg/mL streptomycin (15140-122; Gibco, USA). Cells were incubated in humidified incubators equilibrated with 5% CO_2 at 37°C.

All constructs used in this study were confirmed by DNA Sanger sequencing. Then, the empty vectors or the vectors containing the intact sequence of these genes were transfected into HCC cells using Lipofectamine 2000 (Invitrogen, USA).

The qRT-PCR and/or immunoblotting assays were performed to determine the efficiency of knockdown or enforced expression of genes. The sequences of all PCR primers, shRNAs and siRNAs are listed in Table S5.

Immunoblotting assays

Cells were harvested in phosphate buffer saline (PBS) (4°C), and cell pellets were lysed with NETN buffer containing complete protease inhibitor cocktail (Roche, Germany) and phosphatase inhibitor cocktail (Cwbiotech, Beijing, China). Protein lysates were then subjected to sodium dodecyl sulphate-polyacrylamide gel electrophoresis (SDS-PAGE), and Western blotting assays were performed using the antibodies specific to NRDE2 (1:1,000; 24968-1-AP, Proteintech, China), ATM (1:1,000; 2873T, Cell Signaling Technology, USA), ATR (1:1,000; 2790S, Cell Signaling Technology, USA), CHK1 (1:1,000; 2360S, Cell Signaling Technology, USA), CHK2 (1:1,000; 3440S, Cell Signaling Technology, USA), CK2A1 (1:2,000; 10992-1-AP, Proteintech, China), CK2A2 (1:2,000; 10606-1-AP, Proteintech, China), CK2B (1:2,000; NBP1-06514, Nouvs Biologicals, USA), CK2 phosphorylation (1:1,000; 8738, Cell Signaling Technology, USA), Flag (1:2,000; F3165, Sigma, USA), HA (1:2,000; M180-3, MBL, Japan), Histone H3 (1:1,000; 17168-1-AP, Proteintech, China), MDC1 (1:500; NB100-395, Nouvs Biologicals, USA), MTR4 (1:1,000; 12719-2-AP, Proteintech, China), MYH9 (1:1,000; 11128-1-AP, Proteintech, China), NPM1 (1:1,000; 10306-1-AP, Proteintech, China), RTEL1 (1:1,000; 25337-1-AP, Proteintech, China), pan-p-S/T (1:1,000; AP1067, ABclonal, China), *p*-ATR (1:1,000; 2853T, Cell Signaling Technology, USA), *p*-ATM (1:1,000; 5883T, Cell Signaling Technology, USA), *p*-CHK1 (1:1,000; 2348T, Cell Signaling Technology, USA), *p*-CHK2 (1:1,000; 2197S, Cell Signaling Technology, USA), RANBP17 (1:1,000; DF4379, Affinity, USA), STEAP3 (1:1,000; 17186-1-AP, Proteintech, China) and β-actin (1:5,000; 60008-1-Ig, Proteintech, China), respectively. The β-actin was used as the loading control.

The antibody against p-S378-MDC1 was not commercially available, so we generated it in-house by ABclonal Technology Co.,Ltd. (Wuhan city, China). In brief, the synthetic peptide (AGSD[T-p]DVEE-C) where the T378 located (amino acids 374–382 of MDC1) was conjugated to keyhole limpet hemocyanin (KLH) via a non-native N-terminal cysteine residue and used for immunization in three rabbits to evoke high expression levels of antigen-specific antibodies in the serum. Polyclonal antibodies were then recovered directly from serum. Additionally, we independently generated knockdown clones of MDC1 and MDC1-T378A clones in multiple different cancer cell lines to validate the band specificity and serve as a negative control for the antibodies. Thus, we can perform Western blotting assays using the in-house made antibody specific to p-S378-MDC1 (1:250; custom, ABclonal, China).

High-content functional screening assays

To evaluate the roles of the four candidate HCC-associated genes (*NRDE2*, *RANBP17*, *RTEL1* and *STEAP3*) in HCC cells, the high-content functional screening assays were performed in HepG2 and Huh-7 cells. For each gene, two individual siRNAs were designed and pooled to minimize the possibility of off-target effects. All the siRNAs were purchased from Sigma-Aldrich (Massachusetts, USA), and the sequences are listed in Table S5. The HepG2 or Huh-7 cells were transiently infected by siRNAs against each gene separately for 48 h, and then used for subsequent assays. Each experiment was repeated three times and reported as three independent replicates.

Cell number counting assays. Cells (2×10^3 cells/well) were seeded onto the 96-well plates. The total number of cells in the same field was measured at 24, 48 and 72 h using the bright-field method in the PerkinElmer Opera Phoenix high-content screening system (Massachusetts, USA).

Wound healing assays. Cells were plated in 96-well plates (2×10^4 cells/well). When the cells reached 90% confluence, a scratch was made, and the detached cells were removed by washing with the culture medium. Phase contrast images were obtained in the same field at 24, 48 and 72 h after wounding using the bright-field method in the PerkinElmer Opera Phoenix high-content screening system (Massachusetts, USA).

Immunohistochemistry (IHC) assays

A total of 84 pairs of formalin-fixed, paraffin-embedded HCC tissues and adjacent non-tumor liver tissues of the HCC patients from the General Hospital of Eastern Theater Command (Nanjing city, Jiangsu Province, China) (designated as the TMA cohort) were used for IHC analyses. The clinical information of these HCC patients was provided in Table S8. Tissue microarrays were constructed using the automated tissue arrayer (ATA-27; Beecher Instruments, USA). IHC staining was performed with the antibody against NRDE2 (1:50; 24968-1-AP, Proteintech, China), p-T378-MDC1 (1:250; custom, ABclonal, China) and γ-H2AX (1:500; 05–636, Millipore, USA) on tissue microarray sections after antigen retrieval. The IHC signals were scored as previously described.[77] Briefly, a proportion score was assigned representing the estimated proportion of positive staining cells (0, <5%; 1, 5% to <25%; 2, 25% to <50%; 3, 50%–75%; and 4, >75%). Average estimated intensity of staining in positive cells was assigned an intensity score (0, none; 1, +; 2, ++; and 3, +++). These two parameters were then combined, resulting in an overall score (0–7). Tumors with an IHC score exceeding 3 were considered as NRDE2-high expression group, while the others were considered as NRDE2-low expression group. The IHC assays for the tumor tissues from mice were performed in the same way as those for the tumor tissues from HCC patients.

Publicly available transcriptome and proteome datasets analyses

To assess the expression levels of NRDE2 in tissues of HCC patients, we used the proteome dataset of Chinese HCC patients with HBV infection (CHCC-HBV) from Gao et al.,[78] and four independent mRNA expression profiling datasets in HCCs from The Cancer Genome Atlas (TCGA)-liver hepatocellular carcinoma (LIHC) cohort and Gene Expression Omnibus (GEO; Accession No., GSE76427, GSE56140, GSE63018 and GSE364), along with corresponding clinical information. CHCC-HBV cohort contained 159 pairs of HCC tissues and adjacent non-tumor liver tissues from the HCC patients, and the protein expression levels were measured by isobaric tandem mass tags (TMT)-based global proteomics. TCGA-LIHC cohort contained 351 HCC tissues and 49 adjacent non-tumor liver tissues, and the mRNA expression levels were measured by RNA-seq. GSE76427 contained 115 primary HCC tissues and 52 adjacent non-tumor liver tissues, and the mRNA expression levels were measured by Illumina HumanHT-12 V4.0 expression beadchip. GSE56140 contained 36 liver cirrhotic tissues, 18 center tumor tissues and 15 peripheral tumor tissues, and the mRNA expression levels were measured by Illumina HumanHT-12 V3.0 expression beadchip. GSE63018 contained 9 normal liver tissues, 10 primary HCC tissues and 16 metastasis tissues, and the mRNA expression levels were measured by RNA-seq. GSE364 contained 13 primary HCC tissues without metastasis and 26 primary HCC tissues with metastasis, and the mRNA expression levels were measured by NCI_UniGEM2_HCC. Wilcox rank-sum test was used to compare the protein expressions of NRDE2 between groups. The mRNA expression levels of *NRDE2* were log2-transformed. Mann Whitney U test was used to compare the mRNA expressions of *NRDE2* between groups. The differences of the overall survival (OS) rate between groups were analyzed using the log rank test and Kaplan-Meier curves.

Cells growth and plate colony formation assays

The Cell counting kit-8 (CCK-8; Dojindo, Kumamon, Japan) assays were used to measure the cells growth. Cells were trypsinized and counted by using a handheld cell counter (Millipore, MA, USA). A total of 3×10^3 cells per well were seeded onto the 96-well plates and incubated for 1, 2, 3, 4, 5 and 6 days, respectively. The cells were then incubated with the CCK-8 reagent for 1 h prior to measurement of the absorbance of 450 nm using an enzyme-linked immunosorbent assay (ELISA) plate reader (Thermo Fisher Scientific,

MA, USA). Each experiment was consisted of three replications, and at least three individual experiments were carried out. The recorded curve was shown as the cell index ±standard error of mean (SEM). For plate colony formation assays, cells were seeded into 6-well plates at a concentration of 1×10^3 cells per well and cultured for 2 weeks. At the end of incubation, the cells were fixed with 100% methanol and stained with 0.5% crystal violet-methanol for 15 min (min) at room temperature. The colonies were scanned and counted by Image-Pro Plus 5.0 (Media Cybernetics, USA). Each measurement was performed in triplicate and each experiment was carried out at least three times. The data was analyzed by Student's t test (two-tailed). $p < 0.05$ was considered to be statistically significant.

Cells migration and invasion assays

The abilities of cells migration and invasion were analyzed by a Costar Transwell plates (6.5 mm diameter inserts, 8.0 mm pore size, polycarbonate membrane; Corning, MD, USA). For cells migration assays, a total of 5×10^4 cells were seeded into upper uncoated inserts; and for cells invasion assays, 1.0×10^5 cells were seeded into upper inserts with a Matrigel-coated membrane (Corning, MD, USA). Cells were seeded in serum-free medium and translocated to 10% serum media for 28 or 50 h. After removal of the non-migrating or non-invading cells, the remaining cells were then fixed with methanol for 20 min at room temperature, and stained with 0.5% crystal violet for 15 min. Next, the membranes were washed with PBS and allowed to dry, and an optical microscope (Nikon, Tokyo, Japan) was used to visualize the stained cells in five random fields within each membrane. Cells penetrating the membrane were counted at a magnification of 200×, and the mean was determined. All assays were performed in triplicate, and the experiment was repeated three times. The data was analyzed by Student's t test (two-tailed). $p < 0.05$ was considered to be statistically significant.

Nude mice studies

To assess the effects of NRDE2 on tumor growth and metastases *in vivo*, six-week-old male athymic nude mice (BALB/c background) were randomly divided into the indicated groups (7 mice/group) before inoculation. In subcutaneous implantation mice model, the HepG2 cells transfected with shCtrl or shNRDE2 (1×10^6 cells diluted in 100 μL PBS) were grafted subcutaneously in each side of the mice back ($n = 7$), and the Huh-7 cells transfected with empty vector (Flag-Vector), wild-type NRDE2 (Flag-NRDE2-WT) or mutant NRDE2 (Flag-NRDE2-N377I) (1×10^6 cells diluted in 100 μL PBS) were all grafted subcutaneously in the left side of the mice back ($n = 7$). Tumor volumes were estimated every three days from two-dimensional caliper measurements using the equation $V = (1/2) \times L \times W^2$, where V = volume ($mm^3$), L = length (mm), and W = width (mm). All the mice were sacrificed four weeks later and the tumors were picked out. The tumor tissues were fixed with paraformaldehyde (4%) before dehydration and embedding in paraffin. Paraffin sections were applied for hematoxylin and eosin (H&E) or IHC staining. The anti-NRDE2 (1:50; 24968-1-AP, Proteintech, China) and anti-Ki-67 (1:200; sc-23900, Santa Cruz, California, USA) were used for IHC assays.

In the tail vein injection mice model, a total of 1×10^6 luciferase-tagged Huh-7 cells with or without *NRDE2* knockdown (diluted in 250 μL PBS), and the Huh-7 cells transfected with empty vector (Flag-Vector), Flag-NRDE2-WT and Flag-NRDE2-N377I (1×10^6 cells diluted in 250 μL PBS) were injected into the tail vein of the mice (7 mice/group). The mice were monitored once a week using a bioluminescence imaging. After 4 weeks, the mice were sacrificed. Their livers, lungs and brains were then harvested, fixed in 4% paraformaldehyde, and embedded in paraffin. The sections were stained with H&E and the number of lung metastases was calculated independently by two pathologists.

All animals received human care and all animal experiments were performed in accordance with the guidelines of the Institutional Animal Care and Use Committee of National Center for Protein Sciences (NCPS; Beijing, China).

RNA sequencing analyses

To reveal the underlying mechanism of NRDE2 in HCC, we performed RNA sequencing (RNA-seq) in NRDE2-WT-stably-enforced-expressed, NRDE2-N377I- stably-enforced-expressed and control Huh-7 cells. RNA-seq was performed on Illumina NovaSeq platform at Annoroad Gene Technology Co., Ltd. (Beijing, China).

The RNA-seq reads were mapped to the human genome (hg19) with bowtie2 (v2.3.5.1).[79] Reads mapping to multiple independent genomic locations were assigned to the most abundant biotype of the locations. Transcript quantification was performed using RSEM (v1.3.1) with default parameters.[80] Genome annotations from RefSeq and Ensembl were downloaded from the UCSC genome browser website. For the RNA-seq dataset, DEseq2 (v1.26.0)[81] was used to identify the differentially expressed genes (fold change [FC] $\geq$ 1.2 and adjusted $p < 0.05$). Pathway enrichment analyses of differentially expressed genes and network visualization were performed using Metascape.[82] To determine the biological pathways that are altered after enforced expression of NRDE2, the Gene Set Enrichment Analysis (GSEA) was also performed based on the RNA-seq dataset. The pathways documented in the Molecular Signatures Database (MSigDB, v 7.0) were used in GSEA. Statistical significance was calculated by permuting the gene set 1,000 times with false discovery rate (FDR) < 0.05.

Clonogenic survival assays

HepG2 or Huh-7 cells were plated in triplicate at a density of 3,000 cells per 60-mm plate and incubated for 24 h. Then, the cells were exposed to DNA damaging factors, including ionizing radiation (IR; 0, 1, 5 and 10 Gy, respectively) or camptothecin (CPT; 0, 0.02, 0.1 and 0.5 μM, respectively, for 12 h). Two weeks later, cell colonies were fixed and stained with 0.5% crystal violet in 50% ethanol and counted under a dissection microscope. Statistical data was analyzed by Student's t test (two-tailed). Data was presented as mean ± SEM of three independent experiments.

Cell apoptosis assays

HepG2 or Huh-7 cells were treated with IR (5 Gy) or CPT (10 μM) for 12 h. The cell apoptosis was detected with an APC-conjugated Annexin V/7-AAD Apoptosis Detection Kit according to the manufacturer's instructions (88-8007-74; Thermo Fisher Scientific, MA, USA). In brief, approximately 1×10^6 cells that had been treated as indicated were washed twice with PBS and incubated in 200 μL of binding buffer containing 5 μL of APC-conjugated Annexin V in the dark for 5 min at room temperature. Subsequently, 10 μL of 7-AAD was added, and samples were analyzed with a flow cytometer (BD Accuri C6, CA, USA). Each measurement was performed in triplicate and each experiment was carried out at least three times.

Immunofluorescence staining

HepG2, Huh-7 or U2OS cells were seeded on poly-lysine-coated coverslips and were subject to the indicated treatment. Cells were pre-treated with 0.5% Triton X-100 solution on ice for 5 min prior to fixation. To detect the foci formation of DNA damage response (DDR)-related factors, cells were fixed in 4% paraformaldehyde for 15 min and permeabilized in 0.5% Triton X-100 solution for 5 min at room temperature. Cells were then blocked with 5% bovine serum albumin solution for 1 h and incubated with primary antibody overnight at 4°C. The primary antibodies used here were anti-NRDE2 (1:200; orb221834-CF405M, Biorbyt, USA), anti-γ-H2AX (1:500; 05–636, Millipore, USA), anti-RPA2 (1:200; 10412-1-AP, Proteintech, China), anti-RAD51 (1:150; ab88572, Abcam, USA), anti-53BP1 (1:250; NB100-304, Novus Biologicals, USA), anti-MDC1 (1:250; NB100-395, Novus Biologicals, USA), anti-NBS1 (1:200; 55025-1-AP, Proteintech, China), anti-MRE11 (1:200; 10744-1-AP, Proteintech, China) and anti-RAD50 (1:400; 29390-1-AP, Proteintech, China). The coverslips were washed three times with PBS, and the appropriated secondary antibody was applied for 1 h at room temperature. Corresponding Alexa Fluor 488 (A11029, Invitrogen) and Alexa Fluor 555 (A21428, Invitrogen) were used as secondary antibodies. Confocal images were obtained using a Nikon NIE fluorescence microscope (Tokyo, Japan). NRDE2, γ-H2AX, RPA2, RAD51, 53BP1, MDC1 and NBS1 foci were quantified using the Nikon NIS software (Tokyo, Japan). Foci pictures of each individual experiment were obtained with the same exposure parameters.

Laser micro-irradiation assays

U2OS cells were seeded in glass-bottom dishes, and were pre-sensitized with Hoechst 33342 (Thermo Fisher Scientific, MA, USA) for 30 min. Then, these cells were subject to a 405-nm localized laser beam (70% laser power, 10 s) on an inverted Nikon A1R microscope (Tokyo, Japan). Following laser irradiation, cells were allowed to recover for the indicated time. Then, the cells were fixed with 4% paraformaldehye for 10 min at room temperature. Immunofluorescence staining was then performed and the cells were imaged using the Nikon TIE microscope, and the digital fluorescent images were quantified using the Nikon NIS software (Tokyo, Japan).

Chromatin immunoprecipitation (ChIP) assays

U2OS cells were transfected with 10 μg of Flag-NRDE2-WT vector and 5 μg of I-SceI vector. Cells were collected at the pre-specified time points after transfection (0, 1, 4 and 12 h), and a ChIP assay was performed as previously described.[83] A total of ~1×10^7 cells were crosslinked with 1% formaldehyde for 10 min at room temperature and quenched by the addition of glycine to a final concentration of 125 mM for 5 min. The fixed cells were resuspended in sodium dodecyl sulfate (SDS) lysis buffer (1% SDS, 5 mM EDTA and 50 mM Tris-HCl [pH 8.1]) in the presence of protease inhibitors and 10 mM NAM, then subjected to 3 × 10 cycles (30 s on and off) of sonication (Diagenode, NJ, USA) to generate chromatin fragments of ~300 bp in length. Lysates were diluted in buffer containing 1% Triton X-100, 2 mM EDTA, 20 mM Tris-HCl (pH 8.1), 150 mM NaCl plus 10 mM NAM and protease inhibitors. For immunoprecipitation, the diluted chromatin was incubated with control or specific antibodies (3–5 mg) for 12 h at 4°C with constant rotation, and 50 mL of 50% (v/v) protein A/G Sepharose beads was then added and the incubation was continued for an additional 2 h. Beads were washed with the following buffers: TSE I (0.1% SDS, 1% Triton X-100, 2 mM EDTA, 20 mM Tris-HCl [pH 8.1] and 150 mM NaCl); TSE II (0.1% SDS, 1% Triton X-100, 2 mM EDTA, 20 mM Tris-HCl [pH 8.1] and 500 mM NaCl); buffer III (0.25 M LiCl, 1% Nonidet P-40, 1% sodium deoxycholate, 1 mM EDTA and 10 mM Tris-HCl [pH 8.1]); and Tris-EDTA buffer. Between washes, the beads were collected by centrifugation at 4°C. The pulled-down chromatin complex together with input was de-crosslinked at 70°C for 2 h in elution buffer (1% SDS, 5 mM EDTA, 20 mM Tris-HCl [pH 8.1], 50 mM NaCl and 0.1 mg/mL proteinase K). Eluted DNA was purified with PCR purification kit (Qiagen, CA, USA). The recruitment of NRDE2 to the site of I-SceI was determined by quantitative PCR analysis in which the region from 7 to 315 nucleotides (nt) downstream of the I-SceI site was amplified. The primers used for this step are provided in Table S5.

Neutral comet assays

Neutral comet assays were performed to detect the DSB-induced genomic instability. Briefly, the cells were irradiated with 8 Gy of IR and collected at the indicated time. The comet procedure was applied using the Comet Assay experimental system (Trevigen, USA). Cells were mixed with low-melting agarose and the cell suspension was overlaid on microscope slides. Cell lysis was carried out within the agarose. After lysis, electrophoresis of the DNA trapped in the agarose was performed at 25 V for 30 min. After staining the slides with Propidium Iodide dye for 10 min, images of 60–100 randomly selected cells per sample were captured using an epifluorescence microscope (Olympus IX73; Olympus, Tokyo, Japan) and digital fluorescent images were obtained using the cellSens Standard software (Olympus, Tokyo, Japan). The relative length and intensity of DNA tails relative to heads is proportional to the amount of DNA damage in individual nuclei. These parameters were measured observer-independent and in an unbiased fashion by tail moment quantification with TriTek Comet Score software (TriTek, VA, USA). Exemplary images of single cells from comet slide samples were obtained post analysis.

HR and NHEJ reporter assays

U2OS and HEK293T cells integrated with direct repeat green fluorescent protein (DR-GFP) or EJ5-GFP cassettes were used in the analyses of homologous recombination (HR) or non-homologous end-joining (NHEJ) efficiency, respectively.[29] Briefly, the EJ5-GFP cassette involves two I-Sce1 sites. If NHEJ repair rejoins the two break sites with excision of the intervening segment, the GFP expression is restored. The DR-GFP cassette involves two sequential defective GFP sequences. An I-Sce1 cut site is in the first GFP, and if HR is used with the sister chromatid, the sequence defect can be repaired to a full GFP expression sequence. Cells transiently transfected with the indicated plasmid or siRNA were then transfected with I-SceI expression vector pCBAScel (Addgene, MA, USA) (to induce DSBs) and PCMV-mCherry (Addgene, MA, USA) (as an internal reference to monitor the transfection efficiency). Forty-eight hours after transfection, DSB repair efficiency was analyzed by fluorescence-activated cell sorting (FACS) on a FACSAria flow cytometer (BD Biosciences, CA, USA). HR or NHEJ efficiency was determined by the ratio of cells exhibiting both GFP and mCherry signals to all mCherry cells. All assays were performed in triplicate, and the experiment was repeated three times. The data was analyzed by Student's t test (two-tailed). $p < 0.05$ was considered to be statistically significant.

Immunoprecipitation assays

Cells transfected with the indicated plasmids were collected and lysed in NETN buffer (10 mM Tris-HCl [pH 8.0], 100 mM NaCl, 1 mM EDTA, and 0.5% NP-40) with protease inhibitors (Roche, Basel, Switzerland) on ice for 30 min. Then, cell lysates were subject to mouse monoclonal anti-FLAG (F3165; Sigma-Aldrich, USA), rabbit polyclonal anti-NRDE2 (24968-1-AP; Proteitech, China), rabbit polyclonal anti-CK2A1 (10992-1-AP; Proteintech, China), rabbit polyclonal anti-CK2A2 (10606-1-AP; Proteintech, China) or rabbit polyclonal anti-CK2B (NBP1-06514; Nouvs Biologicals, USA). After rotation for 8 h at 4°C, beads were washed with NETN buffer three times, and samples were boiled with 2× SDS loading buffer and were subject to immunoblotting with the indicated antibodies. For endogenous immunoprecipitation (IP), cell lysates were incubated with the indicated antibody at 4°C for 6 h, and were then subject to Protein A/G beads (Santa cruz, California, USA) for 4 h at 4°C. Beads were then washed with NETN buffer three times, and samples were boiled with 2× SDS loading buffer, and were analyzed by immunoblotting with the indicated antibodies.

Immunoprecipitation in combination with mass spectrometry (IP-MS) assays

The HEK293T cells transiently expressing Flag-tagged empty vector or Flag-NRDE2-WT were lysed in NETN buffer (10 mM Tris-HCl [pH 8.0], 100 mM NaCl, 1 mM EDTA, and 0.5% NP-40) and immunoprecipitated with anti-Flag M2 agarose (M8823; Sigma-Aldrich, MO, USA). After washing four times with the high stringent lysis buffer, the immunoprecipitants were resolved on gradient SDS-PAGE, silver-stained, and subjected to MS sequencing and data analyses. In-solution and in-gel digestion were performed according to a previously published method.[84] Briefly, gel bands were minced and destained with 50% acetonitrile in 50 mM ammonium bicarbonate. Proteins were reduced with 10 mM dithiothreitol (DTT) at 56°C, followed by alkylation with 55 mM iodoacetamide at room temperature in the dark. Trypsin digestion was performed overnight at 37°C with gentle shaking. Peptides were extracted using 1% trifluoroacetic acid in 50% acetonitrile. Samples were vacuum-dried and reconstituted in 0.1% formic acid for subsequent MS analysis. MS analysis was performed using an Easy-nLC 1200 UHPLC coupled to a QExactive HF-X mass spectrometer (Thermo Fisher Scientific, MA, USA). The tandem mass spectra were searched against the human UniProt database (Version 20140922; including 20,193 sequences) using MaxQuant (Version 1.5.3.30).[85] Trypsin was selected as the proteolytic enzyme, and two missed cleavages sites were allowed. Cysteine carbamidomethylation was set as the fixed modification. The oxidation of methionine (M) residues and acetylation of the protein N-terminal were set as the variable modifications. The first search mass tolerance was 20 parts-per-million (ppm), and the main search peptide tolerance was 4.5 ppm. The FDRs of the peptide-spectrum matches (PSMs) and proteins were set to less than 1%.

GST pull-down assays

GST-tagged fusion proteins were expressed and purified from BL21 *E. coli* bacteria and were immobilized on glutathione Sepharose 4B (GE Healthcare, Chicago, USA) at 4°C overnight. Proteins were then eluted with 5-fold volume of glutathione solution (Sigma-Aldrich, MO, USA), and were condensed using 10 kDa protein concentrators (Thermo Fisher Scientific, MA, USA). Proteins were resolved and stocked in PBS containing 5% glycerol at −80°C HEK293T cells transfected with the indicated constructs were treated as indicated. Then, cells were lysed in the NETN buffer (10 mM Tris-HCl [pH 8.0], 100 mM NaCl, 1 mM EDTA, and 0.5% NP-40) with the protease inhibitor and were incubated with the Sepharose immobilized with indicated proteins at 4°C for 8 h. Sepharose was then washed with the NETN buffer three times and was boiled in 2× SDS loading buffer. Samples were subject to immunoblotting with the indicated antibodies.

In silico structure prediction for NRDE2 protein

We performed an *in silico* analysis to predict the functional effects of NRDE2 p.N377I. NRDE2 protein sequences from 12 species were obtained from Uniprot database (https://www.uniprot.org/). We then performed alignment analyses for these protein sequences using Clustal Omega method (v1.2.4) in Jalview (v2.10.5) software. Next, the three-dimensional (3D) model was constructed by the I-TASSER[86] using the protein sequences of NRDE2. Then, the computed 3D structures were used as the starting models for the protein dynamics simulations using DynaMut.[87] The structural image was drawn using PyMOL software (DeLano Scientific, California, USA).

Chromatin fractionation assays

The isolation of NRDE2 or CK2 subunits binding with chromatin was carried out as previously described.[88] Briefly, U2OS cells were treated with CPT for the indicated time, and ~4 × 10^6 cells were harvested and washed with PBS. Cells were resuspended in 200 mL of buffer A (10 mM HEPES, pH 7.9, 1.5 mM $MgCl_2$, 10 mM KCl, 0.34 M Sucrose, 10% glycerol, 1 mM DTT, 10 mM NaF, 1 mM Na_2VO_3, 1 mM PPi and protease inhibitor) containing 0.1% Triton X-100, and incubated for 10 min on ice. After centrifugation (1,300 g at 4°C, 5 min), cytoplasmic proteins were separated from nuclei. The nuclei were then washed once with buffer A and resuspended with 200 mL of buffer B (3 mM EDTA, 0.2 mM EGTA, 1 mM DTT, 10 mM NaF, 1 mM Na_3VO_4, 1 mM PPi and protease inhibitor), and incubated for 40 min at 4°C. Insoluble chromatin was collected by centrifugation (1,700 g at 4°C, 5 min) and washed once with buffer B. The chromatin pellet was resuspended in Laemmli buffer and sonicated for 60 s. The total or chromatin fractions were then isolated for Western blotting assays, and were measured by ImageJ software.

Chromatin tethering assays using the LacR/LacO array system

To test whether CK2 was recruited by NRDE2 to a chromatin region, we performed the single-cell immunofluorescence assay based on *LacR/LacO* system. We used a U2OS-Lac operator (LacO) cell line in which multiple copies of LacO repeats were stably integrated in a euchromatic region of chromosome 1p36 in U2OS cells. For the assays assessing the co-localization of NRDE2 and CK2 subunits at the chromatin, the cells were transiently transfected with GFP-CK2A1 and Myc-LacR-NRDE2. For the assays assessing the interactions among the CK2 subunits, the cells were transiently transfected with GFP-LacR-CK2A1, mCherry-CK2B with empty vector, Flag-NRDE2-WT or Flag-NRDE2-N377I. Then, the immunofluorescence staining and image capture were performed the same as the regular protocol described in the above paragraph with DAPI and antibodies against Myc-tag and FLAG tag. The fluorescent intensity was quantified using ImageJ software based on the images obtained at the identical illumination settings following previously described protocols.[37] The U2OS-LacO cell line was a generous gift from Dr. Fangwei Wang at Zhejiang University (Hangzhou city, China).

Phosphorylation site analysis by liquid chromatography-tandem mass spectrometry (LC-MS/MS)

Cell lysates from HEK293T cells stably expressing Flag, Flag-NRDE2-WT or Flag-NRDE2-N377I were precipitated with acetone and resuspended in 8 M urea. After reduction with DTT and carbamidomethylation with IAA, proteins were digested overnight at 37°C, using the proteases LysC (Wako, Virgini, USA) and dilution with 50 mM potassium phosphate buffer pH 5.8, trypsin (Promega, Wisconsin, USA) and GluC (Promega, Wisconsin, USA). Samples were desalted using SepPak C18 cartridges (Waters, Massachusetts, USA) and phosphorylated peptides enriched with the High-Select TiO2 Phosphopeptide Enrichment Kit (Thermo Fisher Scientific, MA, USA). Proteomic analysis was performed using an Easy-nLC 1200 UHPLC coupled to a QExactive HF-X mass spectrometer (Thermo Fisher Scientific, MA, USA). Peptides were resuspended in Solvent A (0.1% FA), picked up with an autosampler and loaded onto in-house made 50 cm fused silica columns (internal diameter [ID] 75 mm, C18 1.7 mm, Dr. Maisch beads) at a flow rate of 1.5 mL/min. A 90 min segmented gradient of 4%–55% Solvent B (80% ACN in 0.1% FA) over 81 min and 55%–95% Solvent B over 9 min at a flow rate of 250 nL/min was used to elute the peptides. The eluted peptides were sprayed into the heated transfer capillary of the mass spectrometer using a nano-electrospray ion source (Thermo Fisher Scientific, MA, USA). The mass spectrometer was operated in a data-dependent mode, where the Orbitrap acquired full MS scans (350-1,650 m/z) at a resolution (R) of 60,000 with an automated gain control (AGC) target of 3 × 10^6 ions collected within 20 ms (ms). The dynamic exclusion time was set to 20 s. From the full MS scan, the 15 most intense peaks ($z \geq 2$) were fragmented in the high-energy collision-induced dissociation (HCD) cells. The HCD normalized collision energy was set to 28%. LC-MS/MS scans with an ion target of 1.5 × 10^5 ions were acquired with R = 30,000, with a maximal injection time of 54 ms and an isolation width of 1.3 m/z. The raw files were processed using MaxQuant software (version 1.5.3.8) and its implemented viewer and Andromeda search engine.[89] Parameters were set to default values, and Phospho (STY) was added as variable modification. Intensities were scaled to mean of zero and unit variance for separate measurements.

Kinase enrichment and motif analyses

We used the kinase enrichment analysis 2 (KEA2)[90] to infer whether the CK2 kinase activity is regulated by NRDE2 based on the 456 upregulated phosphorylation sites in cells with enforced expression of NRDE2-WT. KEA2 is an online web-based bioinformatics tool which utilizes a database of mammalian proteins/genes with phosphorylation sites and their respective potential kinases. The probable kinase is predicted based on the distribution of kinase-substrate proportions in comparison with the distribution of kinase-substrate in the database. The kinases with FDRs less than 0.05 were defined as the significantly enriched and activated ones. As expected, we observed that CK2 kinase activity is significantly increased in NRDE2-WT-enforced-expressed cells compared to the vector cells. For motif analyses, 456 upregulated phosphor-peptide sequences were submitted to MoMo (v5.3.2) online tool[91] for the identification of over-represented linear signature motifs. The MoMo analyses were performed using the motif-x method and the significance threshold was set to $p < 1.0 \times 10^{-6}$.

5-Bromodeoxyuridine (BrdU) incorporation assays

HepG2 and Huh-7 cells were seeded on coverslips, followed by treatment with IR (2 Gy). At the end of treatment, cells were labeled with BrdU (10 μM) for 60 min, followed by fixation with 80% ethanol and immunostaining with BrdU mouse monoclonal antibody (1:200; 5292, Cell Signaling Technology) and Alexa Fluor 488-conjugated anti-mouse secondary antibody (1:500; A11029,

Invitrogen). The nuclei were counterstained with PI (5 μg/mL), followed by mounting with 90% glycerol containing PI (5 μg/mL). BrdU incorporation was analyzed using the Laser Scanning Cytometer (LSC; CompuCyte Corp, Cambridge, MA, USA), a microscope-based cytometer, as previously described.[92]

Mutational signature analyses

To check whether the *NRDE2* expression levels are associated with the functional HR deficiency in HCC, we queried the prevalence of the Catalog Of Somatic Mutations In Cancer (COSMIC) mutation signature 3 (known to be associated with failure of DNA double-strand break-repair by HR) in HCCs with high or low *NRDE2* expressions. The datasets for the mutation and expression profiles of Chinese HCCs were downloaded from a previous study.[26] The 30 COSMIC signatures categorized by the different combination patterns of 96 tri-nucleotide mutation contexts were downloaded from the COSMIC. The R deconstructSigs package[93] was adopted to determine the contribution of each of the 30 COSMIC signature for each HCC patient. HCCs were stratified into two groups (NRDE2-low expression group, $n = 106$; and NRDE2-high expression group, $n = 53$) by the first tertile *NRDE2* expression level. The differences of mutational signature contributions between NRDE2-low and -high group were assessed using the two-tailed Mann-Whitney U test. $p < 0.05$ was considered to be statistically significant.

Patient-derived tumor xenograft (PDX) mice models studies

The IDMO Co., Ltd (Beijing, China) has successfully established 143 HCC PDX models. Among these 143 models, we obtained three models with NRDE2-N377I, among which, we selected two models for further assays (HCC-1 and HCC-2). Next, we selected two models with NRDE2-WT (HCC-3 and HCC-4). The generation of PDX models was performed by IDMO Co., Ltd. (Beijing, China). Briefly, the fresh HCC tumor tissues were placed in ice-chilled high-glucose DMEM supplemented with 10% FBS, 100 U/mL penicillin and 100 U/mL streptomycin, and were rapidly processed for engraftment. After the removal of necrotic tissues, the tumor specimens were partitioned into 2 × 1 × 1 mm^3 sections with a No.10 scalpel blade under aseptic conditions and were washed 3 times with ice-cold PBS. The tissue fragments were incubated in DMEM medium supplemented with 50% Matrigel (356234; BD, New Jersey, USA), 10 ng/mL epidermal growth factor (PHG0314; Gibco, New York, USA), 10 ng/mL basic fibroblast growth factor (PHG0264; Gibco, New York, USA), 100 units/mL (U/mL) penicillin and 100 U/mL streptomycin for 30 min. Three pieces of tumor tissues with the incubation mix (Matrigel plus growth factors) were subcutaneously transplanted into the right flanks of the male non-obese, diabetic, severe-combined immunodeficiency (NOD/SCID) mice (4–5 weeks old; Vital River Laboratory Animal Technology Co., Ltd., Beijing, China) with a No. 20 trocar. Once the subcutaneous tumor reached 1 cm in diameter, it was minced into pieces (approximately 2 mm^3) and then subcutaneously implanted into the flanks of 4- to 5-week-old nude mice. After the tumor volume reached 100–200 mm^3, the mice induced from each patient were randomly divided into the following four groups: (1) Control (PBS, 100 μL, intraperitoneal injection, once daily for 1 day per week); (2) Oxaliplatin (10 mg/kg, intraperitoneal injection, once daily for 1 day per week); (3) Olaparib (50 mg/kg, oral gavage, once daily for 1 day per week); (4) Combination (Oxaliplatin, 10 mg/kg, intraperitoneal injection; and Olaparib, 50 mg/kg, oral gavage, once daily for 1 day per week). On the 42nd day, the mice were killed by pentobarbital overdose. The investigators were blinded to group medication during experiments and when assessing the outcomes. Animals were housed in a specific pathogen-free mouse facility at the animal center in National Center for Protein Sciences, Beijing (NCPSB). The animal care and experimental protocols were approved by the Institutional Animal Care and Use Committee (IACUC) of NCPSB. The maximal tumor size of PDX mouse model at the experiment endpoint is less than 20 mm in any dimension, in accordance with the IACUC. None of the guidelines was exceeded in any experiment performed. Tumor size was measured using a caliper. Tumor volume in mm^3 was calculated using the formula: Tumor volume [mm^3] = (Length [mm]) × (Width [mm])^2 × 0.52. The tumors were harvested and snap-frozen 24 h after treatment completion.

To establish the primary HCC cell cultures, the HCC tissues from PDX models were minced using a razor blade and digested in collagenase digestion buffer at 37°C for 1 h. Cells were passed through 100 μm and 40 μm cell strainers and centrifuged at 1,200 rpm for 5 min. Cells were incubated in RBC lysis buffer for 2 min and then resuspended in 6 mL medium and spun through 0.5 mL of serum layered on the bottom of the tube to remove the cellular debris. The Contaminated human or mouse haematopoietic and endothelial cells ($CD45^+Ter119^+CD31^+$) were depleted using the biotin-conjugated anti-mouse CD45, CD31 and Ter119 antibodies and separated on a MACS LS column using anti-biotin microbeads. The primary cells were cultured in hepatoma carcinoma cell medium (PreceDo Pharmaceuticals Co., Ltd., Hefei city, Anhui province, China) for validation of mechanism and drug sensitivity.

QUANTIFICATION AND STATISTICAL ANALYSIS

The power analyses

Power analyses were performed using the Power for Genetic Association Analyses (PGA), which is a package of algorithms and graphical user interfaces developed in MATLAB for power and sample size calculation under various genetic models and statistical constraints.[94] Given the HCC prevalence of 0.01‰, 348 cases and 1,749 controls, and p value of 1.0×10^{-5}, the power of our RVAS to identify the rs199890497 (odds ratio [OR] = 12.25; MAF = 0.002) is ~86%, and the power to identify the rs139981430 (OR = 10.70; MAF = 0.002) is ~75%. The powers to identify the rs199890497 and rs139981430 were estimated to be ~67% and ~52%, respectively, given the p value of 5.0×10^{-7}.

Statistical analyses

Differences of cells number, plate colony number, tumor number, foci number, HR and NHEJ efficiency between groups were analyzed using the unpaired *t* tests. Differences of the mRNA expression levels and mutational signature contributions between groups were analyzed using the two-tailed Mann-Whitney U tests. The differences of overall survival rate between groups were analyzed using the log rank test. $p < 0.05$ was considered to be statistically significant. All the statistical analyses, except where otherwise noted, were performed using R software (version 3.6.1).

ADDITIONAL RESOURCES

There are no additional resources.